axioms

IMPACT FACTOR 1.6

Article

The Classical Origin of Spin: Vectors Versus Bivectors

Bryan Sanctuary

Special Issue
Mathematical Aspects of Quantum Field Theory and Quantization

Edited by
Dr. Alexandre Landry

MDPI

https://doi.org/10.3390/axioms14090668

axioms

MDPI

Article

The Classical Origin of Spin: Vectors Versus Bivectors

Bryan Sanctuary †

Department of Chemistry, McGill University, Montreal, QC H3A 0B8, Canada; bryan.sanctuary@mcgill.ca
† Retired Professor.

Abstract

There are two ways of linearizing the Klein–Gordon equation: Dirac's choice, which introduces a matter–antimatter pair, and a second approach using a bivector, which Dirac did not consider. In this paper, we show that a bivector provides the classical origin of quantum spin. At high precessional frequencies, a symmetry transformation occurs in which classical reflection becomes quantum parity. We identify a classical spin-1 boson and demonstrate how bosons deliver energy, matter, and torque to a surface. The correspondence between classical and quantum domains allows spin to be identified as a quantum bivector, $i\sigma$. Using geometric algebra, we show that a classical boson has two blades, corresponding to magnetic quantum number states $m = \pm 1$. We conclude that fermions are the blades of bosons, thereby unifying both into a single particle theory. We compare and contrast the Standard Model, which uses chiral vectors as fundamental, with the Bivector Standard Model, which uses bivectors, with two hands, as fundamental.

Keywords: classical spin; intrinsic angular momentum; geometric algebra; Dirac field; classical correspondence; coherence; bosons; fermions; parity; reflection; Twistor theory; quantum theory; Standard Model; Bivector Standard Model

MSC: 81-10

Academic Editor: Alexandre Landry

Received: 25 July 2025
Revised: 22 August 2025
Accepted: 26 August 2025
Published: 29 August 2025

Citation: Sanctuary, B. The Classical Origin of Spin: Vectors Versus Bivectors. *Axioms* **2025**, *14*, 668. https://doi.org/10.3390/axioms14090668

1. Introduction

When Dirac linearized the Klein–Gordon (KG) equation [1], his anticommuting gamma matrices

$$(\gamma^0, \gamma^1, \gamma^2, \gamma^3) \tag{1}$$

led to the familiar Dirac equation [2] in Minkowski space, which is the Laboratory Fixed Frame (LFF), defined by $(\beta = ct, X, Y, Z)$. However, an alternative linearization exists that Dirac did not know about [3–6]. Instead of Dirac's choice of gamma matrices, the set

$$(\gamma_s^0, \gamma_s^1, \tilde{\gamma}_s^2, \gamma_s^3) \tag{2}$$

also anti-commute where

$$\tilde{\gamma}_s^2 = i\gamma_s^2 \tag{3}$$

introduces a bivector [7]. The subscript s denotes spin spacetime in the Body Fixed Frame (BFF) (β_s, e_1, e_2, e_3). Dirac's linearization led to the identification of two spin-$\frac{1}{2}$ particles with opposite properties, establishing the matter–antimatter pair [8]. The main issue is the negative energy of the antimatter particle, which has never been satisfactorily resolved [9]. The matter–antimatter interpretation is universally accepted. It identifies the two particles

as fundamental fermions of spin $\frac{1}{2}$. This choice leads directly to the Standard Model [10], SM, of particles.

We have shown [4] that the bivector linearization gives a different interpretation that resolves the negative energy issue, the baryogenesis problem, and the EPR paradox [5,6]. The main purpose of this paper is to contrast the bivector linearization from Dirac's choice. We argue that the bivector approach offers an alternative with consequences that may well lead to abandoning the current paradigm based upon chiral fermionic fields of the SM. Rather a Bivector Standard Model, BiSM, is suggested, which replaces chiral fermions as fundamental, with bivector bosons. In this paper, we describe the electron as a physical object with a bivector structure that replaces the usual point particle of the SM.

Figure 1 compares the SM matter–antimatter pair with the BiSM bivector. Both are mirror images, and both have opposite chirality. Dirac proposed two particles, and the bivector model proposes two axes on the same particle.

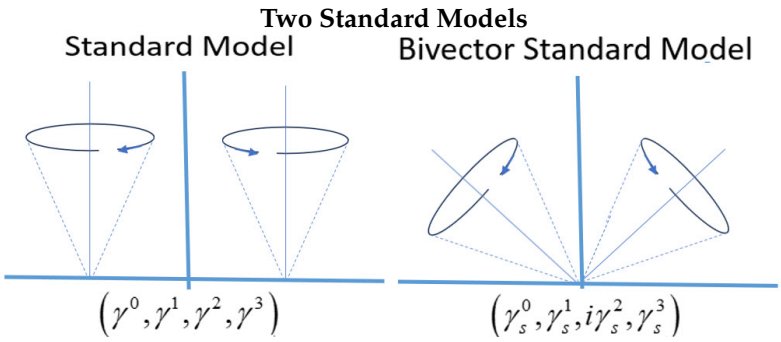

Figure 1. Left: Dirac's matter–antimatter pair of the SM. **Right**: The BiSM showing two counter precessing angular momentum cones on the same particle that form a bivector.

One of the consequences of the bivector spin is that we show for the first time that intrinsic angular momentum has a classical origin. This opens up an entirely different description of the microscopic and gives insight into the fundamental properties of the quantum domain. The description of spin changes from a chiral point particle of intrinsic angular momentum to a well-defined ontic structure: a rotating plane that spans the classical and quantum domains [4]. The consensus is, however, that spin is an intrinsic quantum property without a classical origin. No classical theory has revealed full quantum behavior [11–16]. These approaches universally start with spin as the fermions experimentally observed and use Dirac's matter–antimatter choice.

Hestenes pioneered the use of Geometric Algebra, GA, to reinterpret the Dirac equation by expressing spinors as real multivectors and identifying the internal structure of spin with zitterbewegung (zbw: trembling motion) [17]. This is a rapid, lightlike circulatory motion of the electron at the Compton scale. Spin then emerges from the intrinsic rotation of a localized point-like particle, modeled as a rotor in spacetime algebra, with the complex phase of the spinor reinterpreted as a physical geometric rotation. Both Hestenes's treatment and ours have many features in common. We find internal motion of the electron that likely is the source of a zbw. His interpretation provides a kinetic origin for the rest mass and associates the quantum phase with real rotational geometry. The difference is Hestenes retains the structure of Dirac spinors and relies on the conventional spinor decomposition into electron and positron states. In contrast, the BiSM dispenses with spinors, and models spin as a classical bivector confined in its BFF. It has spin-$\frac{1}{2}$ projections, which emerge from its rotor dynamics of a spin-1 structure. This difference in our approaches, we show here, simplifies the mathematics. Since both approaches use GA, both are focused on geometry.

Building on Hestenes' framework, Doran and Lasenby [7] further developed geometric algebra as a foundation for quantum mechanics (QM) and quantum field theory (QFT).

Their formalism expresses spin states as even-grade multivectors, or rotors, acting on reference vectors, providing a geometric visualization of spin and spacetime dynamics. However, their approach again remains aligned with quantum theory, retaining spinors as fundamental. They preserve complex phase, maintain linear superposition, and rely on operator algebra for measurement.

Muralidhar [18] used GA to study the electron at zero point energy. He finds spin is a bivector governed by classical rotor dynamics, as we do.

Outline

In Section 2, we present the classical mechanics of a bivector and show that its properties correspond to those of quantum spin. We identify a significant bifurcation where classical spinning separates the environment that forms spin states with definite odd and even parity. This transition reflects the change in symmetry from classical reflection to quantum parity.

In Section 3, we describe the symmetry transition between classical and quantum domains and show the correspondence between classical and quantum bivectors.

In Section 4, we interpret the results and describe mechanisms by which external spin chirality relates deterministically to internal chirality, enabling structure formation.

In Section 5, we show the unification of bosons and fermions and the origin of their properties.

In Section 6, the ontological differences between the SM and the BiSM are discussed. We formulate the bivector field as spin 0, 1, and 2 structures. Each is related to a bivector property, which leads to a Lagrangian for both the classical and quantum bivectors.

In Section 7, we show that the superposition of bivectors does not happen and discuss quantization and measurement.

In Section 8, the experimental evidence that supports both the SM and the BiSM is discussed.

2. Classical Spin

The results of this section establish that a classical bivector defines a classical spin-1 boson using no quantum postulates. There is a direct correspondence between classical and quantum spin. This correspondence is taken as strong support that spin is a bivector with two opposite chiral hands.

2.1. A Classical Bivector

Figure 2 shows three different views of spin. On the left is the usual point particle with intrinsic angular momentum, treated as a chiral fermion. On the right is a classical bivector in its BFF with two internal axes (1 and 3), spinning about the 2-axis of linear momentum. In the center is that same bivector but now viewed from the LFF. It is a spinning disc with the internal motion mostly averaged out. The torque, or force, around the 2-axis is in the LFF. In the BFF, that torque becomes the centrifugal force, acting along the bisector of the 1–3 axes, causing them to counter precess. This is internal motion. We also assume that microscopic particles require so little energy compared to its availability that they quickly attain a state of quantum parity by spinning the bivector to high, but not relativistic, frequencies.

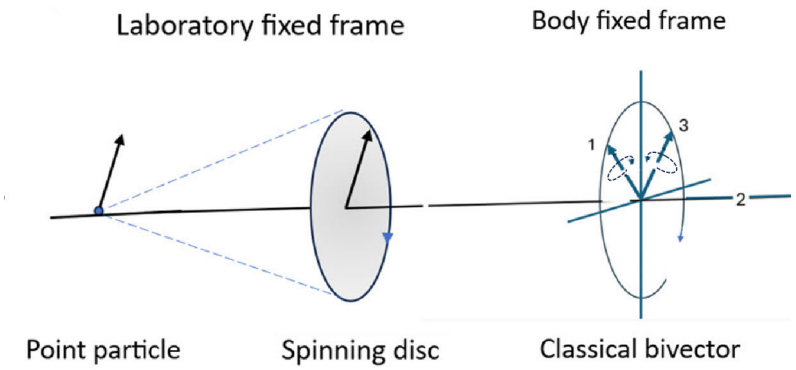

Figure 2. Three views of a spinning object: **Left**: a point particle with spin (LFF), **Middle**: a disc with vector motion (LFF), and **Right**: a classical bivector with internal motion (BFF). In the LFF, the angular momentum is intrinsic, being the projection of the internal bivector motion that is in the BFF, which is unobservable.

2.2. Complementarity

This leads us to the first property shared by classical and quantum bivectors: complementarity. In the LFF, the observer sees a vector precessing around the 2-axis but no internal bivector motion. We see only a projected blur of the internal dynamics, like looking at an engine when lifting the hood. From the BFF, the vector motion around the 2-axis is canceled, but there the internal torques are absorbed, driving the internal bivector dynamics, like the wheels of the engine responding to the applied torque. In the classical domain, there are two complementary views of spin: vector motion around the e_2 axis in the LFF and a coherent bivector motion, $e_1 \wedge e_3$, in the BFF [4].

2.3. Euler's Equations

In the left panel of Figure 3, a bivector is depicted with external vector precession. The two massive orthogonal axes of the bivector are labeled 1 and 3. In response to the vector motion around the massless axis 2, these two axes counter-precess with opposite angular velocities, $\omega = \omega_1 = -\omega_3$. Take the moment of inertia for the external vector as I_{V} and that for the internal bivector as I_{B}. The bivector axes counter precess at twice the frequency of the torque axis, 2; therefore, the rotational energies, $\frac{1}{2}I\omega^2$, for the disc and the two axes are distributed between the vector and bivector in the ratio

$$\frac{E_{\mathrm{V}}}{E_{\mathrm{B}}} = \frac{I_{\mathrm{V}}}{4I_{\mathrm{B}}} \tag{4}$$

a ratio maintained for any precessional frequency of a rigid bivector.

The classical motion is described by Euler's equations. The massless 2-axis provides the torque that turns the bivector either clockwise or counter-clockwise. They are the classical particle's two helicity states. We calculate the motion at fixed frequencies so that there are no external torques and the system is conservative. Euler's equations reduce to the substantial derivative [19]

$$\frac{D\mathbf{S}}{Dt} = \mathbf{S} \times \boldsymbol{\omega} \tag{5}$$

This describes the internal motion by its angular momentum, $\mathbf{S}$, and the constant angular velocity around the 2-axis, giving two equations for the 1 and 3 motions:

$$\begin{aligned} \ddot{\omega}_1 + \Omega^2 \omega_1 &= 0 \\ \ddot{\omega}_3 + \Omega^2 \omega_3 &= 0 \end{aligned} \tag{6}$$

where $\Omega = \frac{\omega}{2}$. The solutions apply conservation of energy and initial equal phases. Two cones of angular momentum are generated, one for each axis. Their interaction plane, 13, is where the two cones are closest and furthest in their orbits, giving

$$\begin{aligned} \mathbf{S}_3 &= e_3 \cos\Theta + e_1 \sin\Theta \\ \mathbf{S}_1 &= e_1 \cos\Theta + e_3 \sin\Theta \end{aligned} \tag{7}$$

These are shown at various angles $\Theta = G/T$, defined as that between an axis, e_i, and the vector, $\mathbf{S}_i$ (Figure 3). The units are radians per second, and G is a gauge to be determined by the system. The period of precessions is $T = \frac{4\pi}{\omega}$. These components are normalized: parallel to the axes is $S_{\parallel} = \cos\Theta$; and perpendicular to the axis is $S_{\perp} = \sin\Theta$ (Figure 3).

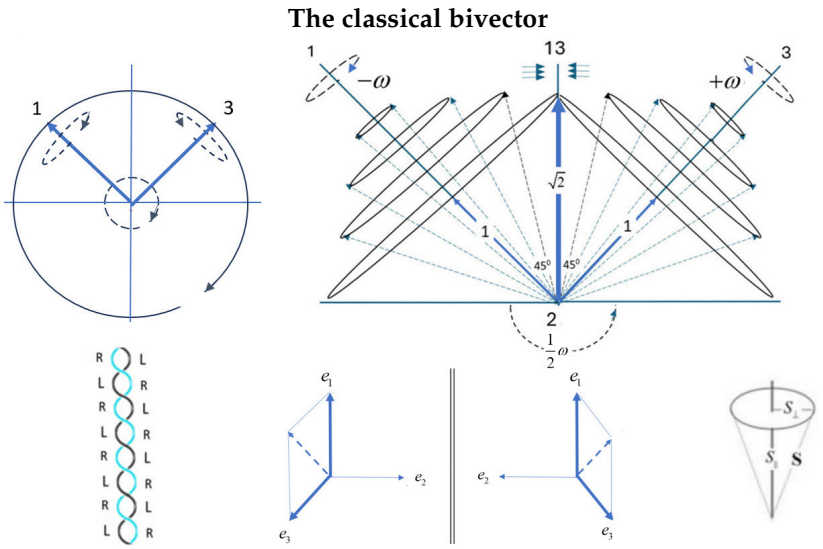

Figure 3. Classical spin bifurcation. **Right**: A classical bivector with axes, 1 and 3, spinning about axis 2 (projecting out of the page). **Left**: The two mirror-image precession states, $\psi^{\pm}$, with opposite chirality. A mirror plane bisects the 1–3 axes. At $\Theta = \frac{\pi}{4}$, the spin magnitude is $\sqrt{2}$, giving a spin-1 boson. **Bottom**: **Left**: Quantum state of even parity showing the loss of reflection within the double helix inside bisector, 31. **Bottom**: **Middle**: Permuting the 1 and 3 labels reverses the handedness of planes. Summing the two frames cancels the torques; subtracting them cancels matter. **Bottom**: **Right**: The cone components $S_{\perp}$ and $S_{\parallel}$, orthogonal and parallel to the precession axis.

2.4. Resonance

This configuration can also be expressed in terms of the angle Φ between the two angular momentum vectors, $\mathbf{S}_1$ and $\mathbf{S}_3$, by

$$\Phi = \frac{\pi}{2} - 2\Theta, \tag{8}$$

giving

$$\begin{aligned} \mathbf{S}_3 &= \mathbf{e}_{31}^{+} \cos\frac{\Phi}{2} + \mathbf{e}_{31}^{-} \sin\frac{\Phi}{2}, \\ \mathbf{S}_1 &= \mathbf{e}_{31}^{+} \cos\frac{\Phi}{2} - \mathbf{e}_{31}^{-} \sin\frac{\Phi}{2}, \end{aligned} \tag{9}$$

where the bisector axes are defined as

$$\mathbf{e}_{31}^{\pm} = \frac{1}{\sqrt{2}}(\mathbf{e}_3 \pm \mathbf{e}_1). \tag{10}$$

With Φ constant, the two orbits resonate between alignment along the bisector, e_{31}^{+}, and cancellation along opposite directions of $\pm\mathbf{e}_{31}^{-}$. Therefore, the tandem and coherent precessional motion results in the two vectors at various fixed values of Φ coming in and out of phase coherence (Figure 3). The mirror plane bisecting the 13 axes reflects them, so neither can distinguish its real counterpart from its own reflection. This figure is shown from $\Theta = 0$ to $\frac{\pi}{4}$, or equivalently from Φ from $\frac{\pi}{2}$ to 0.

From the BFF, top left of Figure 3, the high precessional motion about the 2-axis is canceled, revealing the internal bivector dynamics. The external vector precession and the internal bivector motions are related: for every period of rotation around the 2-axis, the bivector axes counter-rotate by two periods. This is a geometrical example of the double cover of SU(2) over SO(3). The angle Φ remains fixed at constant precession. This resonance within the bivector structure is identified below as a spin-1 boson.

2.5. Geometric Algebra: Bivector Dynamics

A blade is defined as one of the two orthogonal vector axes e_1 and e_3 that are used to define spin (Equation (11) below). Chirality refers to the handedness of this bivector plane, which is determined by left- and right-handed unit quaternions around the 2, or torque, axis [4]. In contrast to the SM, where chirality is projected from the Dirac field using γ^5 [1], here it arises from the opposite chirality of the two blades. These blades are identified as the magnetic numbers of spin, both classical and quantum.

The counter precessing cones of angular momentum, Figure 3, lead to the definition of classical spin as a bivector being the wedge product of the two angular momenta associated with each axis [7]

$$B = \mathbf{S}_1 \wedge \mathbf{S}_3 \tag{11}$$

thereby, also defining their interaction plane, 13. Using Equation (7), the scalar and the wedge products are

$$\begin{aligned} \mathbf{S}_1 \cdot \mathbf{S}_3 &= \sin 2\Theta = \cos\Phi \\ \mathbf{S}_1 \wedge \mathbf{S}_3 &= e_2 \cos 2\Theta = e_2 \sin\Phi \end{aligned} \tag{12}$$

Normalized $\mathbf{S}$ gives a unit quaternion structure of a scalar and bivector, which we express as the geometric product [7], of the two angular momenta

$$\begin{aligned} Q_B(\Phi) &= \mathbf{S}_1\mathbf{S}_3 = \mathbf{S}_1 \cdot \mathbf{S}_3 + \mathbf{S}_1 \wedge \mathbf{S}_3 \\ &= \exp(e_2\Phi) = \cos\Phi + e_2 \sin\Phi \end{aligned} \tag{13}$$

Classical spin is a bivector, Equation (11), and the geometric product, Equation (13), describes its dynamics as a classical rotor.

The unit vector e_2 is normal to the 31 plane, and $Q_B(\Phi)$ gives rotation around the 2-axis, which is manifest in the LFF as a spinning disc. There is no vector component in the BFF. This quaternion also gives a measure of scalar and bivector contributions at different angles. The scalar part gives a measure of its mass, and the bivector part gives coherent rotational kinetic energy from the two counter precessing axes. At $\Theta = \frac{\pi}{4}$, $(\Phi = 0)$, the scalar part is maximized to 1, and the two axes, 1 and 3, meld, which cancels their precessions, leaving scalar mass. Equation (4) shows that the ratio of the rotational kinetic energies is fixed. As the internal frequency goes to zero, the external precession slows and stops. In isotropy, all kinetic energy is converted to mass, which is the only property it displays. It is still a bivector. At this angle, call the BFF the rest frame and the mass the rest mass. We identify this maximally confined structure to have the classical electron radius $r_e \approx 2.82 \times 10^{-15}$ m. We refer to this as an inert electron, without charge, denoted by e_B.

Cold Dark Matter

Inert electrons are candidates for Cold Dark Matter. They have no electromagnetic component. Most electrons in the universe might never have become part of atoms. Rather they might have possibly been produced in vast quantities during the Big Bang, far exceeding the number needed to balance baryons. These electrons never entered into interactions, never radiated, and never annihilated, remaining inert. They do not need positive charge to balance them. Over cosmic time scales, they might be trapped by galaxies. Although speculative, one can envision they form inert halos of mass that are predicted by simulations [20].

The Double Helix

From Figure 3, the angular momentum along the bisector, 13, has no physical axis and is a purely resonant state: the eye of a tornado along 13. The analogy is apt but with an extra twist. The eye of a vector tornado is a region of calm and lower energy yet surrounded by a vortex of high precessional energy. In contrast, the bivector tornado is due the two axes melding into an eye of left and right chiralities intertwined in harmony. There is no vortex, only a scalar directed along the bisector with calm everywhere else. It forms the double helix of the electron, Figure 3, lower left. Therein Nature stores the defining properties of an electron: angular momentum, $\hbar$, electron charge of the usual fermion electron, e_F^-; and its mass, m_o. At $\Phi = 0$, and for the first time, we assign this state the magnetic *quantum* number $m = 0$. The two blades, $m = \pm 1$, have folded together. Not only is reflection lost, but opposite blade properties also cancel. This depicts the quantum state of the electron, which exists at $\Phi = 0$. When an inert electron encounters a polarizing field, its properties of spin (chirality), helicity, charge, and mass emerge as observed. The two blades are forced into a polarizing state of $\Phi = \frac{\pi}{2}$ that is indistinguishable from a fermion.

The quaternion, $Q_B(\Phi)$, is also a phase that changes sign when 1 and 3 labels are swapped. This symmetry operation shows the 1 and 3 labels are indistinguishable, allowing for both the clockwise and counter clockwise helicity around the 2-axis.

2.6. A Classical Boson of Spin-1

This resonant and scalar state is formed from the coherent coupling of the two perpendicular components, $S_\perp$, one from axis-3 and one from axis-1. As seen from Figure 3, the component from axis-1, $S_\perp$, projects onto the 23 plane, while the axis-3 component projects onto the 12 plane. Any angle Θ will give a spin-1, but the maximum value occurs when $S_\parallel = S_\perp$ at $\Theta = \frac{\pi}{4}$. We normalize these cone projections. The angle between the projected component and the bisector, 31, is $\theta = \frac{\pi}{4}$. A spin is formed from these two components, which resonates giving a state of length $\sqrt{2}$. Using the quantum definition for the angle, θ, between a spin axis and its cone, we obtain

$$\cos\theta = \frac{m}{\sqrt{s(s+1)}} \xrightarrow{s=1} \frac{1}{\sqrt{2}} = \cos\frac{\pi}{4} \tag{14}$$

which is identified as a purely classical spin-1. Moreover, this particle is rapidly spinning, averaging out all anisotropies, and obeying Bose–Einstein statistics. We are justified in calling the classical spin a boson. Since the spin-1 is a result of the coupling of the two blades, we assign a spin of $\frac{1}{2}$ to $\mathbf{S}_1$ and $\mathbf{S}_3$.

2.7. Special Relativity

Using the angular momentum of an electron, $\frac{h}{2}$, its mass, and a radius defined by the de Broglie wavelength in atomic systems of $\lambda = 1.94 \times 10^{-11}$ m, we found a rim velocity

of $\omega r = v_{\text{rim}} = 8.9 \times 10^6$ m/s, or about $0.03c$, is attained. This allows us to determine the gauge, G, for an electron. At $\Theta = \pi/4$ let $T = T_e$,

$$G = \frac{\pi}{4} T_e = \frac{\pi}{4} \times \frac{\lambda}{0.03c} = \frac{\pi\lambda}{0.12c}$$
$$\Theta = \frac{\pi\lambda}{0.12cT} \tag{15}$$

Relativistic effects [21] are determined by the relativistic angular frequency, ω^c, which is given by

$$\omega^c = \gamma(v_{\text{rim}})\omega = \frac{\omega}{\sqrt{1 - \frac{v_{\text{rim}}^2}{c^2}}}, \tag{16}$$

where γ is the Lorentz factor. The divergence of ω^c reflects relativistic time dilation effects, not an actual physical increase in the intrinsic angular velocity ω. At higher precessional frequencies, to compensate for time dilation, the observed precessional frequency ω^c decreases. The condition $v_{\text{rim}} = \omega r < c$ must be satisfied. As $\omega^c \to 0$ and $\lambda \to \infty$, the system ceases to spin, and energy is converted to mass. Here, $\lambda = v_{\text{rim}}/\omega^c$ is the effective coherence length or wavelength associated with the relativistic angular frequency. However, this usual explanation of the relativistic limit can never be approached by an electron because the quantum domain occurs first.

The Quantum and Relativistic Limits

Due to the intertwining of the two chiralities, the cones cannot pass through one another and instead become confined as mass along the bisector, 13. The quantum limit, therefore, occurs at $\Theta = \frac{\pi}{4}; \Phi = 0$. At this limit, the energy is

$$E = \frac{1}{2} m_{\text{eff}} v_{\text{rim}}^2 + \frac{1}{2} m_{\text{eff}} (-v_{\text{rim}})^2 \tag{17}$$
$$= m_{\text{eff}} v_{\text{rim}}^2 \to m_0 c^2 \tag{18}$$

with $m_{\text{eff}} = \gamma(v_{\text{rim}}) m_o$ in terms of the internal rest mass giving

$$\gamma(0.03\text{c}) = \frac{1}{\sqrt{1 - 0.03^2}} = 1.00045 \tag{19}$$

At $v_{\text{rim}} = 0.03c$, the electron is far from its relativistic limit. At this point, however, all rotational kinetic energy is fully confined into its double helix in Figure 3. The quantum domain exists only at $\Phi = 0$. After the two chiralities have melded, the addition of more internal energy is not possible. Instead, it propels the entire structure through space, shifting the dynamics from internal confinement in the BFF to external forward propagation in the LFF. The relativistic limit, $v_{\text{rim}} \to c$, can never be approached internally, thereby capping the rest mass.

This establishes a geometric origin and physical mechanism for the quantum and relativistic limits. The Lorentz factor becomes a geometric measure of the quantum limit and differs for types of particles. In contrast to the SM, which treats mass as intrinsic and structureless, the BiSM shows that rest mass arises from a structured, geometric state formed at the quantum boundary.

3. Correspondence and Parity

In this part, we formalize the correspondence showing how classical spin maps to quantum operators and how parity bifurcation emerges geometrically. Planck's constant is identified from the structure.

3.1. Parity from Reflection

The symmetry of our domain, the LFF, is different from the bivector symmetry of the BFF. This transition at $\Theta = \frac{\pi}{4}, \Phi = 0$, defines when reflection becomes parity. To see this significant symmetry transition, note our Right Handed Frame (RHF) domain has three spatial dimensions of definite chirality. We can never get to the Left Handed Frame (LHF) and see only a mirror reflection of our RHF. The matter that is used to make a machine and the torques that make the wheels turn are both in our RHF domain. The bivector, in contrast, has one axis in a LHF and the other in the opposite RHF. They are mirror or reflective states, $\psi^{\pm}$, in opposite handed frames (Figure 3). They form a chiral pair, a left and right hand of Nature. In complete contrast to us, the bivector does not see its reflection in the mirror plane but its real opposite chiral hand.

Reflection evolves to positive parity at $\Phi = 0$ when the two angular momenta lock into their double helix of mass inside their reflection plane. Reflection is lost, as shown in Figure 3, lower left. Up until the double helix of mass is formed, the left and right frames are separate and reflection preserved, but, as shown, left and right reflections intertwine along the bisector, which defines the quantum domain. Therefore, that figure shows that the two reflections add, and they can also be subtracted.

$$\Psi^{\pm} = \frac{1}{\sqrt{2}}(\psi^{+} \pm \psi^{-}) \tag{20}$$

Since the system is a two-dimensional plane, 31, a permutation operator, P_{13}, interchanges left-handed planes and right-handed planes, so $P_{13}(e_1, e_2, e_3) = (e_3, e_2, e_1)$, giving

$$P_{13}\psi^{\pm} = \psi^{\mp} \tag{21}$$

Therefore, a LHF and a RHF, shown in the bottom panel of Figure 3, combine into states of definite parity with the permutation, P_{13}, being the parity operator,

$$P_{13}\Psi^{\pm} = \pm\Psi^{\pm} \tag{22}$$

Adding gives even parity and cancels the torque axis 2; subtracting gives odd parity and cancels the massive axes, 1 and 3, thereby separating matter from force. Thus, the emergence of quantum parity from classical reflection is a necessary consequence of the bivector structure.

3.2. Classical–Quantum Correspondence

The classical domain is described by a continuous mixture of vector and bivector motion, forming a single classical convex set. As the angle Φ decreases, the symmetry shifts from classical reflection to quantum parity. As $\Phi \to 0$, the classical system transitions to two distinct convex sets with opposite parity. It is not the bivector that changes but the symmetry of the environment inside the BFF that causes a phase transition from reflection to parity.

As the angle Φ varies, vector $V_c(\Phi)$ and bivector motion $B_c(\Phi)$ are geometrically mixed forming a field over a classical convex set [22]:

$$\Sigma_c(\frac{\pi}{2} \geq \Phi \geq 0) = V_c(\Phi) + B_c(\Phi) \tag{23}$$

where

$$\begin{aligned} V_c(\Phi) &= \sin\Phi e_2 \\ B_c(\Phi) &= \cos\Phi e_1 \wedge e_3 \end{aligned} \tag{24}$$

To be clear, the vector motion about the 2-axis is expressed by $V_c(\Phi)$ in the LFF, and the complementary internal bivector motion is expressed by $B_c(\Phi)$ in the BFF.

As Φ varies, the system undergoes a continuous transition in its parity structure from external $p_{13} = -1$ to internal $p_{13} = +1$, where p_{13} is the eigenvalue of the parity operator, P_{13}. As an initial and slowly turning torque is applied, $\Phi = \frac{\pi}{2}$, and the system is dominated by external torque in the LFF, which turns the 2-axis either way with chirality (helicity) of left or right. The symmetry is dominated by reflection until the cones form a double helix when reflection is lost. These two parity states coexist in different domains: force (LFF) and the responding mass–energy (BFF). At the critical $\Phi = 0$, the system reaches maximum mass confinement, and all motion stops. The external torque can then only cause an increase in forward propagation. The system is at its rest frame with rest mass in a state of positive parity. The double helix can accept no more energy, external spinning halts, and reflection symmetry is extinguished. This pure parity state $p_{13} = +1$ dominates, and the LFF registers no torque and so has no parity. This further defines the quantum domain of the electron. Thus, parity is present and co-exists simultaneously with complementary roles. The geometric product, Equation (13), quantifies this dynamic by giving the balance between internal labile energy and mass.

We express this as a symmetry transition from reflection to parity giving two convex sets each with definite parity. Before this, the only symmetry is reflection, like we experience. However, at $\Phi = 0$, the symmetry of the system changes to parity:

$$\Sigma_q(\Phi = 0) = V_q \oplus B_q \tag{25}$$

where $\oplus$ is the Minkowski sum [23], which combines elements from different convex sets. The quantum vector field with odd parity is separated from the bivector field with even parity. These give the quantum components that define quaternion, or Q-spin [4]:

$$\begin{aligned} V_q &= \{\sigma\} \\ B_q &= \{i\sigma\} \end{aligned} \tag{26}$$

There is no Φ dependence in the quantum domain since the two cones are locked along their bisector. The bivector form of the Dirac equation also undergoes bifurcation [4], and this is summarized in Appendix A where the Clifford algebra changes from $Cl(1,3)$ to $Cl(2,2)$.

3.3. Continuous Versus Discrete Symmetry

Classical–quantum correspondence, based on their commutation relations, is usually expressed by

$$E \leftrightarrow i\hbar\frac{d}{dt},\ p \leftrightarrow -i\hbar\frac{d}{dr},\ J \leftrightarrow -i\hbar\frac{d}{d\theta} \tag{27}$$

This now extends to spin angular momentum, giving a complete quantum–classical correspondence. We replace the classical spin, Equation (23), with its corresponding quantum operators, a Pauli vector and a Pauli bivector, giving the classical correspondence of quantum spin:

$$\begin{aligned} e_1 \wedge e_3 &\leftrightarrow i\sigma_2 \\ e_2 &\leftrightarrow \sigma_2 \end{aligned} \tag{28}$$

We note, however, a fundamental difference in that the variables, E, p, and J become classical as $\hbar \to 0$. Moreover, those variables are continuous, whereas parity is a discrete symmetry. Spin does not become classical as $\hbar \to 0$. The quantum domain exists only at $\Phi = 0$ from which quantum effects emerge. We define Planck's constant as the internal

angular momentum of an electron at $\Phi = 0$. In the BiSM, Planck's constant is not postulated but arises as the angular momentum associated with this state of pure positive parity.

The only difference between the SM and the BiSM lies in the treatment of spin: the former gives two vectors in a Hilbert space with superposition, while the latter is a real structure in our spacetime with no superposition. The correspondences in Equation (27) follow from Noether's theorem [24], and quantization arises from their commutation relations. These remain unchanged in the BiSM. It is, however, widely misunderstood that the Fourier relations between continuous variables are examples of superposition. They are not. For superposition to apply, the variables, such as spin components in the SM, must be represented within the same Hilbert space. There is no superposition between conjugate pairs since they are dual elements belonging to distinct spaces. Such cases are examples of representation theory [25], which does not imply that the system exists simultaneously in those basis states. Rather, they represent the same information in complementary domains. Wave–particle duality does not imply superposition. This point is made by Ballentine [26] and Dirac [27] and is consistent with von Neumann's treatment [28]. Expansions over continuous variables are not physical superpositions but rather representations of a continuous state in a chosen basis.

Essential to the BiSM are the two frames, the LFF and the BFF. They differ in their relative precessions, which begs the question concerning the Quantum Reference Frame (QRF) [29,30]. With no superposition in the BiSM, there are no quantum effects that manifest in the QRF, considerably simplifying representations [25]. Likewise, superselection [31] is not a feature of the BiSM. We found no experimental evidence where quantum effects of the reference frame have been observed.

Calculation of Planck's Constant

Consider a mass equal to the electron mass, $m_e = 9.109 \times 10^{-31}$ kg, moving at a rim velocity $v = 8.9 \times 10^6$ m/s along a circular path of radius $r = 8.17 \times 10^{-11}$ m. Using the classical formula for angular momentum,

$$h = m_e \, r \, v, \tag{29}$$

we obtain

$$\begin{aligned} h &= 9.109 \times 10^{-31} \cdot 8.17 \times 10^{-11} \cdot 8.9 \times 10^6 \\ &\approx 6.62 \times 10^{-34} \, \text{J·s} \end{aligned} \tag{30}$$

which matches the accepted value of Planck's constant entirely from independent physical quantities. The value of r is about 1.5 times larger than the Bohr radius placing it within atomic dimensions. It is also roughly 34 times the Compton wavelength $\lambda_C \approx 2.43 \times 10^{-12}$ m and approximately 2.9×10^4 times the classical electron radius $r_e \approx 2.82 \times 10^{-15}$ m.

It may seem counter-intuitive that the radius required to generate Planck's constant reaches atomic dimensions extending the radius to be larger than the Bohr radius. However, this radius is on the scale of the actual spatial extent of electron orbitals. In the hydrogen atom, the average radius for finding the electron in the ground state 1s orbital is $\langle r \rangle_{1s} = 1.5 a_o = 7.94 \times 10^{-11}$ m, using the Bohr radius. Our calculated spin radius, $r \approx 8.17 \times 10^{-11}$ m, is close. This suggests that the angular momentum structure of the electron occupies the same scale as the atomic orbitals and gives physical justification for the delocalized and cloud-like appearance of electron orbitals. Orbitals are where the electron's mass extends, not where a point particle electron might be. We, therefore, interpret

atomic orbitals as diffuse mass from spatial distributions of rotational kinetic energy which manifest as quantized angular-momentum modes.

In QM, orbitals are probability densities for localizing a point particle electron in space. These map out the orbitals, giving the probability of finding the point particle somewhere in these probability clouds. Instead, in the BiSM, the extended internal geometry is the electron's spin structure, not the probability of its location. The electron is not a point-like carrier of charge but a dynamically coherent angular momentum structure. In the BiSM, the orbital is a manifestation of a single electron.

Quaternion Spin

We replace the classical vector and bivector, Equation (23), with their corresponding quantum operators, Equation (28), giving the classical correspondence of quantum spin, which we call quaternion or Q-spin [4,5],

$$\Sigma = \sigma + \underline{\underline{\underline{\varepsilon}}} \cdot i\sigma \equiv \sigma + \underline{\underline{\underline{\mathbf{h}}}} \tag{31}$$

in terms of the coherent helicity operator, $\underline{\underline{\underline{\mathbf{h}}}}$ [5], which is an element of physical reality. The inclusion of helicity transforms the spin operator, Σ, into a unit quaternion. The external vector motion, σ, is observed in the LFF, while the bivector, $i\sigma$, describes internal bivector motion in the BFF. This quaternionic structure of Σ forms the quantum analogue of the classical spin bivector (Equation (23)).

The EPR Paradox

Including correlation between vectors and bivectors, Equation (31) resolves the EPR paradox [5,6,32]. EPR coincidence experiments [33–35] measure correlation, not polarization. As such, both vectors and bivectors provide contributions. Bell's theorem [36,37], refers to one classical convex set, whereas polarization and coherence are two complementary convex sets in the BiSM. This is shown in Figure 4, where the full EPR correlation is given by a function that is cosine-like, $-\cos(\theta_a - \theta_b)$, and which also violates Bell's Inequalities. However, the triangle is the simulation of the correlation between two vectors, giving a CHSH [33], of 2. The mustache is the simulation of the correlation between two bivectors, with CHSH = 1. Bell's Inequalities are not violated when applied twice: once for vectors and again for bivectors. Bell's theorem is different from his inequalities, which in his own words is [36]

> "If [a hidden-variable theory] is local it will not agree with quantum mechanics, and if it agrees with QM it will not be local."

The simulation in Figure 4 disproves this by showing the "violation" is a result of bivector correlation and not a consequence of non-locality and entanglement [5,6,33–36,38,39]. The Bell–Kochen–Specker theorem [36,40] discusses contextuality showing that contextual hidden variable theories are compatible with QM. Although this theorem is insightful, it is not applicable to Q-spin since their conclusions are only valid for three dimensions or more, and Q-spin is two-dimensional in spin spacetime. There are, therefore, no hidden variables, but as we show below, contextuality plays an important role in the BiSM.

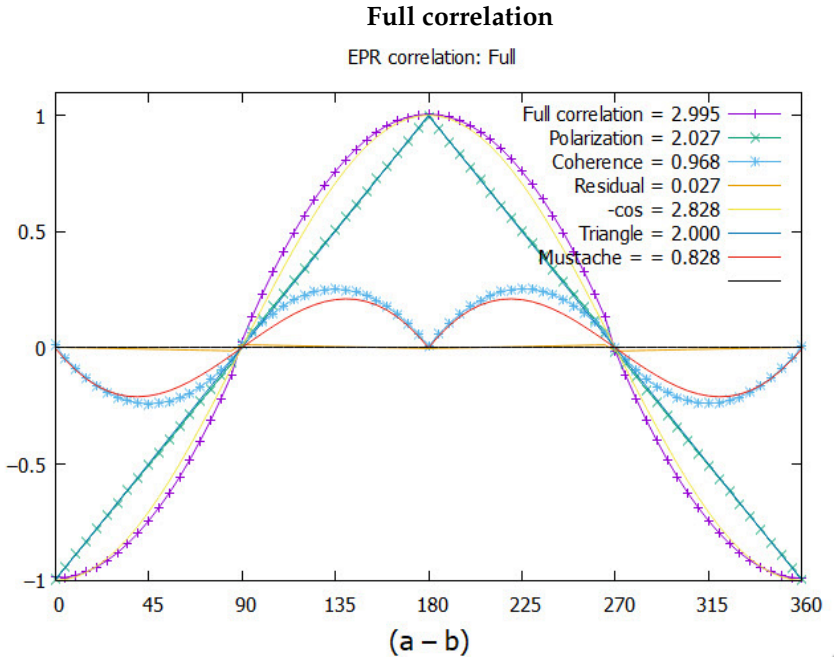

Figure 4. Plotting EPR correlation versus the angle difference $(\theta_a - \theta_b)$. The points give the results of the simulation. The CHSH values are listed, and the full correlation is the sum of polarization (the triangle) and the coherence (the mustache). Note the hardly discernible residual polarization correlation along the horizontal axis, which shows the contribution extracted from the polarization, $2.027 - 2.000 = 0.027$.

4. Interpretation

The magnitude of the classical spin-1 is a direct consequence of the orthogonality between the bivector axes 1 and 3. The two measured outcomes of spin is a result of the geometric structure as one blade or the other aligns with the field. The classical bivector spin-1 exists for all values of Φ but maximizes when the wedge product $B = \mathbf{S}_1 \wedge \mathbf{S}_3$ has a magnitude of $\frac{1}{\sqrt{2}}$. The maximum construction of a spin-1 boson is shown in the middle panel of Figure 3.

4.1. Hammers, Wrenches, and Matter

Parity and reflection lead to mechanisms for bosons interacting with targets, driven to form states of fixed parity. Depending on the field alignment, a boson can hammer the target, torque it, or add a mass quantum to a structure. Assume that the bivector is in an isotropic environment, free of fields, so it has a state of $m = 0$. When a field is present, the two axes are pulled apart, and one aligns. The interaction of the boson with the target is simply described as the interaction between that bivector axis, $\mathbf{S}_i$, and a field component, $\mathbf{B}(\theta_a)$, on the target:

$$e^{\pm i\omega t}\mathbf{S}_i \cdot \mathbf{B}(\theta_a)e^{\mp i\omega t} \rightarrow 1. \tag{32}$$

The two vectors are normalized. Both the target and spinning disc are coplanar, and in that measurement plane, the field is oriented at angle θ_a, which is depicted by the long arrows in Figure 5. There are two general cases: the field is within the interaction plane, 13, the upper arrow of the right panel, or it lies outside the interaction plane, the lower arrow. In Equation (32), the field is outside the interaction plane, and the blade and field vectors join to form mass because the frequencies are opposite. If the frequencies are coherent, they generate a torque (Figure 5).

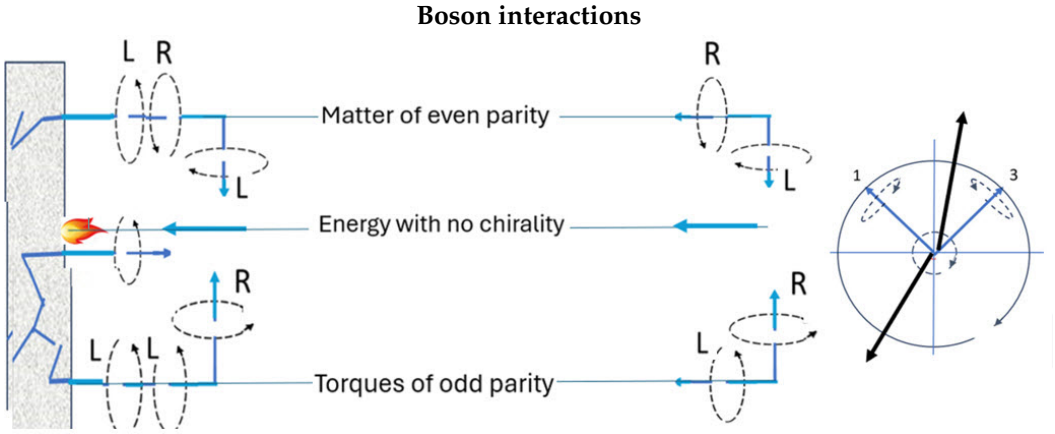

Figure 5. Three manifestations of bosons: When the incoming boson and the target have opposite chirality, they meld into matter of even parity. When their chiralities are equal, they combine to create a greater torque of odd parity. These require the polarizing field be outside the 13 interaction plane, lower arrow on the right. If the polarizing field lands within the interaction plane, 31, upper arrow on the right, then a massive quantum impinges on the surface with no chirality. The long arrows denote two positions of the polarizing field vector: one in the interaction plane and the other outside of it.

4.2. Determinism

The determinism of the BiSM follows from the relationship between the chirality of the 2-axis and the chirality of the interacting blade. This is shown, for example, in Figure 3, top left, where the leading blade is expressed as follows. Clockwise precession, L, of the 2-axis ensures the leading blade is 3, with ccw, R, chirality. It is this blade that will first encounter the field vector, $\mathbf{B}(\theta_a)$. Reversing the 2-axis to ccw, R, Figure 3, top right, ensures the leading blade, now 1, has cw, L, chirality. As the boson approaches the target surface, Figure 5, it becomes polarized and aligns into Larmor precession about a field axis. This is shown in the upper panel where the boson has R chirality, and melds into matter. If the chirality of the 2-axis is reversed, the lower panel, both have the same L chirality and generate a torque. This way, the external chirality (helicity) deterministically picks the chirality of the leading blade. The 2-axis is spun by the unit quaternion, which has definite chirality. However, the helicity so generated is not a Lorentz invariant, so the sense of the helicity depends on the rest frame. Therefore, the chirality of the spin should be determined at the source in the LFF and not from free flight observation.

The dynamics are intuitive with one bivector axis aligning with Larmor precession and the other randomizing. The boson can also deliver a quantum of energy that impinges on the target. If the field lies within the interaction plane, 31, Figure 5, then the blades remain folded, leaving a spin-1 being a massive arrow that strikes the target.

We note building matter is an asymmetrical process due to melding opposite chiralities into a double helix, thereby obeying Fermi–Dirac statistics, and reminiscent of the chiral mechanisms that are common in chemistry and biochemistry. It is also possible for the source to determine the boson's helical phase relative to the target, thereby specifying where the boson will meet the field. In processes where particles move over relatively short distances, their landing site on the target plane can be deterministic. This requires the boson to be released at a specific distance from the target, thereby determining where the boson is relative to the field by $\cos(\theta_a - \theta + 2n\pi)$, where θ is the initial phase of the helicity at the source, and the integer n is the number of periods between the source and the target. If the bosons arrive randomly at the target, then one quarter of the time they will hammer the surface with arrows of quanta, and three-quarters of the time, fermionic blades will couple with the target to build matter.

5. Unification of Bosons and Fermions

5.1. Internal Mass–Energy

Mass and rotational kinetic energy are distributed within the bivector internal motion. In contrast, a massless point particle has energy only associated with free precession about the 2-axis. This free motion defines massless particles with energy given by $E = pc$. There is no internal energy. In contrast, bivector structure hosts energy and mass, which is mass–energy confinement. This internal bivector motion distinguishes massive from massless particles. In the BiSM, the mass–energy relation is a geometric effect of internal structure and dynamics.

We have shown [4] that the solution of the 2D Dirac equation gives opposite energies for the 1 and 3 axes [4]:

$$E_{\pm} = \pm\sqrt{m^2 + p_3^2 + p_1^2} \tag{33}$$

This is entirely different from the conventional Dirac interpretation where the three energy components, p_i, are from the linear momenta of two-point particle with opposite energy. Rather, the expression (Equation (33)) emphasizes that internal mass–energy arises from the confined internal rotational kinetic energy between the 1 and 3 axes within the BFF. This trivially avoids the negative energy of the SM antiparticle. Moreover, the internal structure prevents singularities associated with point particles. These lead to divergences in the SM as interactions occur at or close to zero separation, where the energy densities can become infinite. Renormalization is then applied to absorb these singularities into redefined masses and charges [41–48]. However, these divergences are not physical and arise from mathematical artifacts of structureless point particles. By assigning structure and finite size to the bivector, energy densities remain finite. The divergences that plague point-particle theories, requiring renormalization, are avoided in this geometric model.

5.2. Emergence of Spin

In the presence of a polarizing field, the two axes are pulled apart, and Φ is no longer zero. The $m = 0$ state would resist this forceful process. The spin properties of kinetic energy, charge, and helicity emerge in response. As one blade aligns in the field, its partner randomizes. The spin has all the properties of a fermion, and only in such states can spin be measured. The outcomes, however, are not chiral particles of spin-$\frac{1}{2}$ but the polarized blades of a boson. Fermions are emergent in the BiSM. This unifies fermions and bosons and eliminates the need for fermions as fundamentals in the BiSM.

An electron is a boson in free flight with no charge; a fermion in a field with charge; with an anyon transition between them, [49],

$$e_F^-(\text{anisotropy, fermion}) \overset{\text{anyon}}{\underset{\text{transition}}{\longleftrightarrow}} e_B(\text{isotropy, boson}) \tag{34}$$

Anyons require 2+1 dimensions, exactly the structure of bivectors spin which is an oriented 2D plane. This links directly to braid theory [50], from which the double helix can be viewed, topologically, as a two-strand braid, [51]. This transition is governed by the anisotropy or isotropy of the environment and is, therefore, contextual [52,53]. In isotropic conditions, the bivector remains folded and behaves as a boson; in anisotropy, the blades unfurl, producing a fermionic appearance. Therefore, the BiSM need list only bosons.

5.3. Emergence of Charge

The mass-only free-flight boson is not a sphere but a microscopic massive bivector frame that hosts no kinetic energy until encountering an anisotropic field. In doing so, the 2D structure gains internal kinetic energy, and helicity emerges, Equation (4). With helicity, mass, and spin accounted for, the remaining property is its charge.

In the SM, charge arises from the generator of the $U(1)_{em}$ gauge symmetry, which numerically obeys the Gell–Mann–Nishijima relation [54,55]. The hypercharges are fixed by anomaly cancellation and by experiment, which lack a geometric derivation.

We first note, the bivector electron has well defined properties which are identical for all. As the electron starts off with external torque motion in the LFF, the parity eigenvalue is $p_{13} = -1$. With increased precession, parity moves to the quantum state of $p_{13} = +1$ whence the double helix quantum state is formed. The final state, composed of a braid of left and right chirality, must have the identical linking number, (the number of twists), for all electrons in order for the properties to be identical. Linking number may play a fundamental role in distinguishing properties of particles.

We expect, therefore, charge to emerge from the inert electron as the internal motion of the two blades responds to the external polarizing field. It forces one of the blades to align with the field and its partner to average out. In that process, a dynamic phase shift is introduced between the two blades which can be interpreted as charge. In the following, we propose a possible mechanism for this process, which takes place in the BFF.

There, the two blades counter-precess with opposite sense at the same frequency, $\pm\omega$. As the blades are forced apart, a time-dependent phase shift, $\chi(t)$, develops. The two reflected angular momenta on the cones move in and out of phase coherence in tandem. After a small time δt, one advances by $+\omega\,\delta t$ and the other by $-\omega\,\delta t$ so their separation changes by $2\omega\,\delta t$. Hence, $\dot{\chi} = 2\omega$ and

$$\chi(t) = \chi_0 + 2\omega t \tag{35}$$

with units of radians. We call this tandem difference a chord, which depicts the oscillatory motion between the two angular momenta, $\mathbf{S}_1$ and $\mathbf{S}_3$, on their cones. That is, the internal angular momenta resonate at 2ω. This is expressed by $\chi(t)$ with energy of $\Delta E = 2\hbar\omega$ from Equation (33).

At $m = 0$, within the double helix, the magnetic moments cancel, which we express by

$$\mu_1(t) = \mu_0 e^{\,i\omega t} \text{ and } \mu_3(t) = -\,\mu_0 e^{-\,i\omega t} \tag{36}$$

With a field present, causing counter precession, their sum gives an internal oscillatory magnetic moment with a sinusoidal envelope,

$$\mu_{13}(t) = \mu_1(t) + \mu_3(t) \;=\; 2I_{13}\,\mu_0 \sin(\omega t) \;=\; 2I_{13}\,\mu_0 \sin\Big(\frac{\chi(t)}{2}\Big) \tag{37}$$

The chord angle χ lies between $0 \le \chi \le \pi/2$, due to fixed orthogonality. The magnetic moment, too, forms a bivector. Let b_1 and b_3 be the unit directions of the blade dipoles (so $\mu_1 = \mu_0 b_1$ and $\mu_3 = \mu_0 b_3$). Their geometric product is

$$b_1 b_3 = b_1 \cdot b_3 + b_1 \wedge b_3 \;=\; \cos\chi + I_{13}\,\sin\chi. \tag{38}$$

Here, I_{13} is the unit bivector for the plane 13. It plays an identical role as the imaginary i since $I_{13}^2 = -1$, but in GA, the unit bivector defines the plane upon which the imaginary properties manifest. This is consistent with the metric tensor of Clifford algebra $Cl(2,2)$ of our treatment, [4]. The imaginary i alone simply indicates a 90-degree rotation. There are two motions: the chord oscillation in the BFF, like the zbw, Equation (37), and the geometric product giving external motion in the LFF, Equation (38).

The applied field creates an imaginary component as seen in both above equations. We suggest it signifies the presence of charge. An example is found in the covariant derivative in QFT ($\partial_\mu \to D_\mu = \partial_\mu - ieA_\mu$). In geometric algebra, when the axes are fully separated

at $\chi = \pi/2$, the scalar part vanishes, and only the imaginary bivector remains, which we identify as positive or negative charge:

$$q(\chi) = p_{13} q_0 \sin\chi, \tag{39}$$

with the sign set by $P_{13} I_{13} = p_{13}\, I_{13}$ with $p_{13} \in \{+1, -1\}$, which denotes the chirality of the 13 plane. Its magnitude is $\sin\chi$. The charge of the electron, Equation (39), is $q_0 = e_F^-$ and attained at $\chi = \frac{\pi}{2}$.

The internal dynamics of the magnetic moment chord represents the difference between reflective points on the cones (Equation (37)). This oscillatory motion is within the BFF and time averages, giving only a projection in the LFF. However, the boson displays its charge, and one blade is now polarized, displaying both chirality and its permanent magnetic moment of μ_0, ready to couple to the external field. It is now the electron we know and consistent with known results.

As an aside, the chord phase is related to the energy gap between Dirac's electron–positron pair. Recall the rim speed, $v_{\text{rim}} \approx 0.03\, c$, from Equation (15). The precession rate and internal length scale satisfy $v_{\text{rim}} = \omega\, r$. If we assume Compton precession, $\omega = mc^2/\hbar$, then the internal energy difference is $\Delta E = 2\hbar\omega = 2mc^2$ (Equation (33)). This is the minimum gap energy in Dirac's theory and demonstrates a difference between the two models, consistent with the same parameters.

Additionally, the zbw [17] produces a fluctuation at twice the Compton frequency between positive and negative states. This is consistent with Equation (35), which shows internal oscillations between the two opposite blades, also with the double frequency.

The mechanism is purely geometric, independent of quantum postulates. When $\chi = 0$, the blades are in phase and the system is neutral, $m = 0$. When the field drives the blades to orthogonality, $\chi = \pi/2$, then $m = \pm 1$, and the electric charge emerges from internal bivector geometry. It need not be postulated. While this is not yet a complete model of charge, it provides a credible mechanism relating an internal geometric phase to the emergence of electric charge.

5.4. Photons Are Massless Bivectors

We propose that both the photon and the electron possess a bivector structure yet represent different physical phenomena. So far, we have treated the spin-1 electron using Classical Mechanics on a bivector, and energy is distributed between mass and rotational kinetic energy. In contrast, the electromagnetic field propagates at the speed of light. As the mediator of electromagnetic force, the photon must also be massless. Maxwell's equations replace Classical Mechanics. As a bivector, the photon has a free and unconfined electromagnetic structure, which defines a kinetic surface:

$$\mathrm{s}_{\text{kin}} = \mathbf{E} \wedge \mathbf{B} \tag{40}$$

where $\mathbf{E}$ and $\mathbf{B}$ are the electric and magnetic fields of the photon. This dynamic surface propagates in the direction of the Poynting vector [7]:

$$\mathcal{P} = -\frac{1}{\mu_0} I(\mathbf{E} \wedge \mathbf{B}) \tag{41}$$

where I is the unit pseudoscalar in 3D space. With this, the Faraday bivector field is written using Equation (5.166) of [7]:

$$\mathbf{F} = \mathbf{E} + I\mathbf{B} \tag{42}$$

Squaring this field gives the two Lorentz invariants of the electromagnetic field:

$$F^2 = E^2 - B^2 + 2I(\mathbf{E} \cdot \mathbf{B}) \tag{43}$$

For a freely propagating electromagnetic wave (i.e., a classical photon), the conditions, ($c = 1$),

$$\mathbf{E} \cdot \mathbf{B} = 0 \quad \text{and} \quad |\mathbf{E}| = |\mathbf{B}| \tag{44}$$

are valid, giving $F^2 = 0$. This condition reflects the orthogonality and equal magnitudes of **E** and **B** in free space. The field is not "zero" but rather balanced and propagating energy. This condition implies the photon can carry no mass because the two blades **E** and **B** remain orthogonal, leaving only a kinetic surface.

Both electrons and photons are modeled as spin-1 bosons in free flight. However, the electron converts all of its energy into confined rotational motion, producing mass. This does not pose a problem since electrons usually act over relatively short distances and accelerated by their Lorentz force. Photons, in contrast, mediate interactions between massless fields, where mass would hinder propagation. When a photon enters a field, for example, near a molecule, the orthogonality between **E** and **B** is lost. The field becomes non-null, and energy can convert to mass, slowing the photon for easier capture. This is seen from Equation (43), $F^2 \neq 0$. Since a photon lacks a magnetic moment, it does not give rise to electric charge like an electron, distinguishing photons from electrons in the BiSM framework.

6. Ontology

Up to this point, we have developed the classical mechanics of bivectors without relying on quantum postulates. The essential difference between the SM and the BiSM is ontological. The SM and QM are successful, particularly in many-body systems, including spectroscopies, solid-state physics, and nuclear structure, where angular momentum addition and algebraic methods are applied. These successes are shared by the BiSM in the Fermion approximation, discussed below, but with an ontological shift. In this section, we outline the main contrasts in particle interpretation, algebraic foundations, spin construction, and field formulation.

6.1. Particles

The SM describes particles as abstract, chiral point-like excitations of quantum fields, while the BiSM treats them as finite, structured objects with internal geometry, like molecules. In contrast to point particles, in the BiSM, they are structured, finite systems characterized by internal bivector dynamics. Spin, mass, and charge emerge from the geometry and motion of counter-precessing blades within the particle. These properties are not imposed through abstract symmetries but arise naturally from internal resonance and energy. Every particle has a definable geometry, making it real and visualizable in real space.

Chirality in the SM is algebraically defined and treated as fundamental. Left- and right-handed versions behave differently under weak interactions. In the BiSM, a particle with only one chirality cannot physically exist. This property is rather a blade of its spin-1 bivector. The distinct chiral particles of the SM are replaced by the polarized blades of the BiSM. The balance of left–right chirality of a bivector is not present in fermion particles with only one hand.

6.2. No Neutrinos

Beta decay [56–58] can be expressed as a neutron in a nucleus decaying into a proton by emitting a beta particle, i.e., a fermion electron, and an anti-neutrino:

$$\begin{array}{c} {}^{1}_{0}\mathrm{n} \rightarrow {}^{1}_{1}\mathrm{p} + e^{-}_{F} + {}^{0}_{0}\bar{\nu} \\ \frac{1}{2} \rightarrow \frac{1}{2} + \frac{1}{2} + \frac{1}{2} \end{array} \tag{45}$$

The inability of beta electrons to conserve spin angular momentum and energy led Pauli [58,59], to hypothesize neutrinos. They are fermions with neither mass (initially) nor charge, and with the fermion axis colinear to the axis of linear momentum. They violate parity, being only left handed while antineutrinos are only right handed. Pauli's neutrino are indistinguishable from a single blade cut off from a bivector.

Boson beta electrons, e_B, in contrast, have a spin of 1, internal structure, and no charge. The latter should account for the energy distribution and, therefore, not violate the conservation of energy. The spin-1 boson balances the spin without a neutrino:

$${}^{1}_{0}\mathrm{n} \rightarrow {}^{1}_{1}\mathrm{p} + e^{-}_{F} \rightarrow {}^{1}_{1}\mathrm{p} + e_B \tag{46}$$

$$\frac{1}{2} \rightarrow \frac{1}{2} + 1 \tag{47}$$

Note that the equation appears to not conserve charge, but as the electron leaves the neutron, it initially carries a balancing negative charge in its $m = \pm 1$ states and is a Fermi electron. When far enough away, in free flight Equation (34), the external charge disappears into its chirality. The charge is not lost, but stored within the double helix, and restored as needed. From the LFF its parity is odd. The reasons to reject neutrinos are: equivocal experimental evidence; indefinite parity properties; no sinks to remove them; and now the boson electron obviates the *raison d'être* for fermion electron neutrinos.

This contradicts experimental evidence [60–66]. However, no neutrino has been directly observed. Detection is based upon collision products using the SM, with the electroweak gauge symmetry of SU(2) × U(1). A great advantage, and disadvantage, of QFT is the range of processes that can be constructed. Whether real or hypothetical, neutrinos are consistent with a number of processes, such as inverse beta decay; scattering and recoil experiments; nuclear reactions, ^{37}Cl decaying to ^{37}Ar; and Cherenkov radiation [60], created from neutrino interactions when charged particles move faster than the speed of light in a medium. Today, Cherenkov radiation [65] and inverse beta decay [66] are most common.

Nonetheless, using these method, over enormous fluxes of neutrinos, very few such indirect events are recorded. A typical experiment over a year with a calculated flux of, say, 10^{15} neutrinos, only a few hundred indirect events are detected. Although steps are taken to avoid them, we suggest these are due to other events, like cosmic rays, natural radioactivity or instrumental noise. Muons from cosmic showers can produce similar secondary particles to Cherenkov radiation. However, neutrino detectors use several methods, such as deep placement underground, coincidence rejection, muon veto systems, and directional analysis, to reduce the chances of misidentifying cosmic ray signals as neutrinos. Despite these precautions, cosmic rays still represent a significant challenge, with an extensive literature [67–74]. We suggest current data is not conclusive evidence that neutrinos exist.

6.3. Parity Is Not Violated in the BiSM

In the 1950s, Yang and Lee [75] suggested that the weak force may not obey parity which motivated experiments. The 1956 experiment, conducted by Wu Chien-Shiung

and her colleagues [76], confirmed parity violation, which was a crucial yet disrupting contribution to the field [56]. Parity conservation was a widely accepted principle that stated that the mirror image of a physical process should be indistinguishable from the original process in the real world. Parity violation is as weird as quantum weirdness.

Wu's experiment focused on the beta decay of cobalt-60 nuclei, emitting a beta electron (e_F^-), and an electron antineutrino (Equation (45)). According to the law of parity conservation, this process should be isotropic in all directions. However, Wu's team observed a clear asymmetry in the emitted electrons' distribution. Wu stated [76],

> "If an asymmetry in the distribution between θ and $(180 - \theta)$ ... is observed, it provides unequivocal proof that parity is not conserved in beta decay."

The BiSM suggests an alternate explanation of her data due to a beta particle being a boson of odd parity in isotropy, e_B. As discussed in the last section, this immediately shows that for beta decay, the antineutrino is not needed to balance spin, and the internal structure conserves the energy. Therefore, without neutrinos, we assert the beta decay process for cobalt is given by

$$^{60}_{27}\text{Co} \rightarrow ^{60}_{28}\text{Ni} + e_B + 2\gamma \tag{48}$$

In the experiment [76], the cobalt sample was placed in a solenoid that produced a polarizing field along the polar axis and which can be reversed. Wu measured the gamma rays, the distribution of which is the same as that for the beta particles. Equatorial counts were used to normalize the polarization. By reversing the current in the solenoids, the experiment detected an asymmetry in the number of counts between the north and south. The mirror symmetry is not faithful and parity is violated. This is shown in Figure 6. The first column is the real world. The second column depicts the parity transformations, and the last column performs a π rotation needed so the first and third columns are mirror images. If parity is conserved, the expected distribution must be symmetrical, which is shown in the first row.

(a) Since the magnetic field, the cobalt spin, and the fermion electron are all axial vectors, they are symmetrical under parity. As stated above, Wu expected this result if parity is conserved.

The real-world image in the second row,

(b) This is what Wu actually observed, an asymmetrical distribution of beta events. Performing the same transformations as in (a), it is a clear that the mirror reflection is not faithful, showing parity is violated. For this reason, it is concluded that parity is violated in Nature. In contrast, if the beta particle is a boson electron with odd parity, then row

(c) of Figure 6 shows the real-world data are faithfully reproduced for any distribution observed. Parity is not violated under in the BiSM.

This result is surprising but not unsatisfying. At the time, Wu's experiment was also a surprise. Considerable effort is, and has been, devoted to understanding the implications of parity violation. The 1956 results caused a paradigm shift in physics, and ended the belief that all physical processes are symmetric under mirror reflection. This has consequences. The laws of physics are not completely uniform under some symmetry transformations. Important components in the SM are a direct consequence. Parity of the weak force is not conserved. Charge violation emerged so that CP is conserved, along with theories based upon parity violation. Reversing the interpretation of the Wu data underscores part of the paradigm shift anticipated by replacing the SM with the BiSM. Although tumultuous, it simplifies our view of Nature.

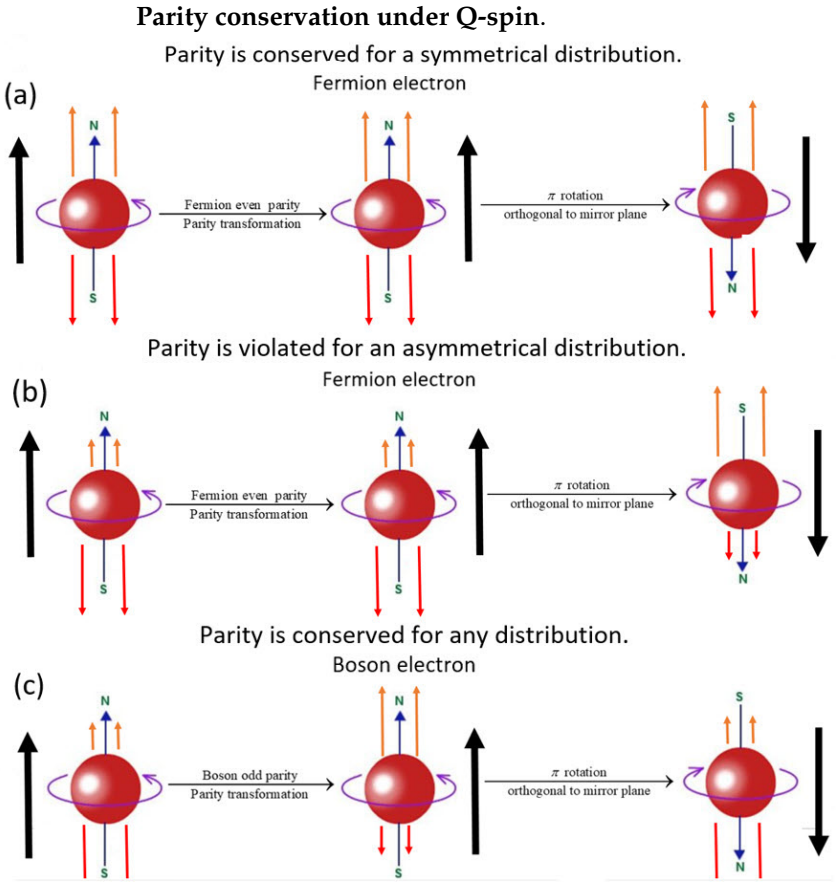

Figure 6. The cobalt nuclei are the large spheres. The thick arrows denote the magnetic fields. The small arrows are beta particles. The first column is the real world, and the last is the mirror world. (**a**) For a symmetrical distribution of beta fermion electron, parity is conserved. (**b**) For a asymmetrical distribution of beta fermion electron, parity is not conserved. (**c**) Using boson electrons, parity is conserved for any distribution.

If the bivector spin structure is accepted, then the spin of a neutrino cannot physically create one-handedness without the other and would violate conservation laws. This, we assert, is impossible and is a fatal argument against the physical existence of neutrinos. Our classical bivector calculation suggests that definite parity is a defining property of a particle. The classical concepts of parity, P, charge, C, and time, T, are always conserved, and we assert these properties are maintained in the quantum domain. Neutrinos and parity violation are non-physical artifacts of the SM.

6.4. Lie Versus Clifford Algebra

The SM is based on Lie algebras to define particles and interactions. Spin is imposed via spinor representations, and gauge invariance is enforced through covariant derivatives and gauge fields. Electron–positron pairs are controlled by raising and lowering operators on that fermion field [1]. In the BiSM, the mathematical framework is Clifford, or Geometric Algebra [7]. Spin is not a vector of intrinsic angular momentum but a spinning bivector plane. In the SM, spin is postulated and expressed as eigenvalues of abstract operators. In the BiSM, geometric structures host energy, like a tuning fork, and these are described by operators and eigenvalues.

In order to show the basic difference between the SM and the BiSM, we compare how each forms spin states. Figure 7 [77–80] distinguishes between the parentage schemes of forming higher spins using Lie algebra of fermions and the geometric algebra of bivectors. An explanation of the figure is given in Appendix B. These two schemes reflect the double-

cover relationship between SU(2) and SO(3), as seen from the interleaved half-integral entries on the left. The SM uses this spinor-based Lie algebra scheme. The acceptance of fermions as real chiral particles is due to a measured blade being indistinguishable from a fermion. Use of them as fundamentals in the SM increases the number of particles, as seen by comparing the boxed on the right (four irreps.) and equivalent on the left (twelve irreps.). In the BiSM, chiral fermions are reinterpreted as projections of a spin-1 bivector structure, which eliminates the need to postulate point-like spin-$\frac{1}{2}$ entities. We retain the parentage scheme on the right. However, we go a step further by replacing the input vectors with bivectors. Instead of constructing states from vectors $\mathbf{r} \in \mathbb{R}^3$, we use bivectors such as $B = \mathbf{S}_1 \wedge \mathbf{S}_3$, representing oriented planes and hypervolumes in geometric algebra.

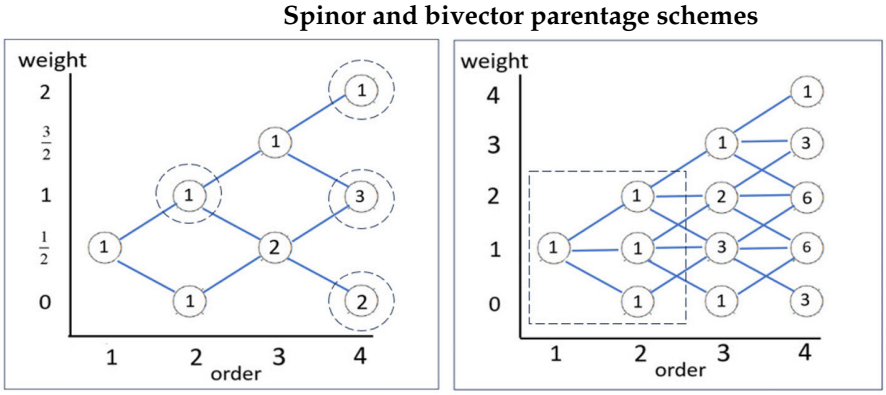

Figure 7. Left: Spinor-based SU(2) construction of higher spins. **Right**: Vector based construction using SO(3) symmetric traceless tensors.

This approach avoids proliferation of particles due to arbitrary algebraic constructions, which the use of vector fields over a Hilbert space permits.

6.5. The Bivector Field

The bivector field lies within the particle and is defined by the classical spin expression (Equation (11)). This internal field does not extend over spacetime. The geometric product, Equation (13), describes energy–mass balance from the scalar mass term and the kinetic energy wedge product term. The field is generated from the BFF. In the LFF, only the projection of the bivector motion is visible, revealing only intrinsic vector angular momentum. The structure of the field is illustrated on the right of Figure 7, where spin-2 arises from the tensor product of two spin-1 bivectors. This product decomposes into three representations: spin-0 and spin-2 in the BFF and spin-1 in the LFF.

Spin-0 (Scalar): Formed by the scalar product of two bivectors,

$$\mathbb{S} = B_1 \cdot B_2 \tag{49}$$

this term is invariant under rotations and has no directional dependence. The mass of a spin-1 boson arises from this term and replaces the Higgs mechanism.

Spin-2 (The wedge of two spin-1s): Unlike vector-based constructions, bivectors are antisymmetric and do not naturally form symmetric traceless tensors. Instead, the quadrupole moment arises from the pure 4-blade component of the bivector product,

$$Q = B_1 \wedge B_2 \tag{50}$$

This is in four-dimensional space, e.g., as seen in the BFF. The quadrupole is depicted in the middle of Figure 8. The upper panel shows the 4-blade geometry, and the lower panel shows the scalar spin-0 component. The full geometric product is,

$$\begin{aligned} B_1 B_2 &= B_1 \cdot B_2 + B_1 \wedge B_2 \\ &= \text{scalar} + \text{4-blade} \end{aligned} \tag{51}$$

If the bivector planes share a common axis, say e_2, then a wedge of two equal components is zero, and the 4-blade-spin-2, content vanishes. The remaining scalar, spin-0, is again mass. The spin-2 part comes from the two planes, B_1 and B_2, being transverse. It then has five states $m = 0, \pm 1, \pm 2$. The $m = 0$ state in isotropy, and the $m = \pm 1, \pm 2$ states are the dynamic components. The BiSM is a candidate for the description of gravity with two pairs of antisymmetric components of the Riemann curvature tensor, represented by a spin-2 as the wedge product of two bivector spins, $B_1 \wedge B_2$.

Geometric spin structures.

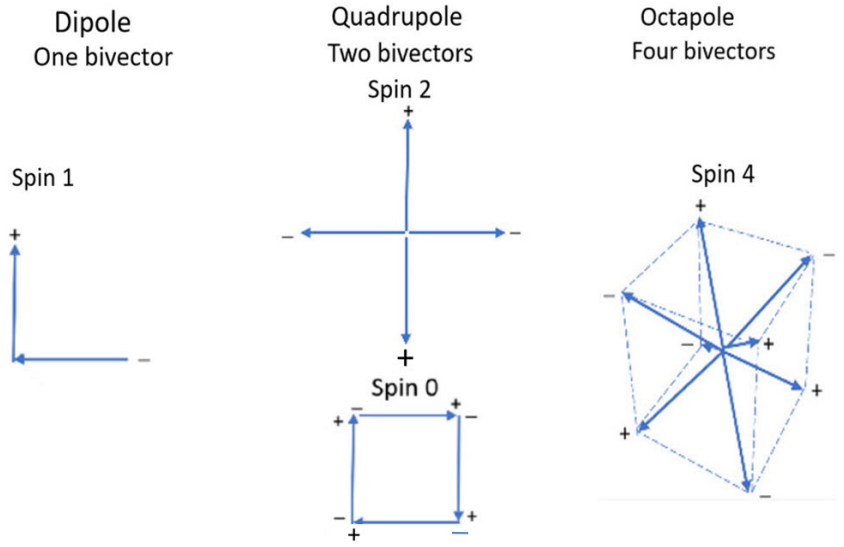

Figure 8. Geometric structures by combining bivectors.

Spin-1 (Triplet State): A 4-blade bivector becomes a spin-1 by contracting Equation (51), with another bivector. Previously, we described the 2D spin disc as coplanar with the field plane. Express this measurement plane by $f \wedge n$ where n is a reference axis, and f is a force. In the absence of a field, the spin-1 averages to zero due to external precession. In a field, the antisymmetric part of the geometric product, Equation (51), is written

$$T(f, n) \equiv (B_1 \wedge B_2) \cdot (f \wedge n) \tag{52}$$

Together they give a spin-1 bivector which can couple with with an external field, similar to Equation (32). Therefore, we include coupling to an external current, J^μ with strength g, expressed as usual,

$$\mathcal{L}_{\text{int}} = g J^\mu A_\mu \tag{53}$$

where A_μ denotes the potential.

To complete the field structure, we define a field-strength bivector, $G_{\mu\nu}$, analogous to how the Faraday tensor $F_{\mu\nu}$ organizes electric and magnetic fields,

$$G_{\mu\nu} := \partial_\mu A_\nu - \partial_\nu A_\mu. \tag{54}$$

The corresponding kinetic term in the Lagrangian is,

$$\mathcal{L}_{\text{kin}} = -\frac{1}{4} G_{\mu\nu} G^{\mu\nu} \tag{55}$$

These field structures together formally express a basis for building the classical and quantum Lagrangians in the BiSM. Similar forms are found in [1,81].

7. Quantization and Measurement

Quantum theory was originally developed in response to observed discreteness, blackbody radiation, photoelectric effect, and atomic spectra, and it was natural to model the system as quantized from the outset and develop a theory distinct from classical systems. The classical–quantum correspondence of spin was unknown, so spin was postulated. In the SM, spin is treated as a label on a state vector in a Hilbert space. Superposition and collapse follow as mathematical necessities, not physical processes.

In QM, bivectors are present but largely unrecognized. The geometric product of Pauli matrices is the basis for our treatment [82].

$$\sigma_i \sigma_j = \delta_{ij} + \epsilon_{ijk} i \sigma_k \tag{56}$$

which combines a scalar and a bivector. However, only the first term is measured in the LFF, leading to a two-state outcome, with the concomitant Lie algebra structure, commutators, and superposition. Including the bivector changes the spin to Equation (31) [5]. The first term describes the measured vector spin as one axis up and the other axis down. The second term cannot be measured in polarized experiments, and the most visible contribution is seen in Figure 4, where bivector correlation accounts for the violation of Bell's Inequalities [32].

We first discuss Lagrangians, with the classical system providing the internal and external motions. This is not quantized. Rather, after parity symmetry is established in the BFF, there are two distinct quantum Lagrangians: one for the BFF and the other for the LFF.

7.1. Lagrangians

The scalar and wedge product, Equation (12), and the quaternion phase, Equation (13), form the basis for building the classical Lagrangian [1,7,19,83–85]. Each term corresponds to a physical contribution: internal energy, force as torque, and mass coherence. Together, they describe the internal dynamics of the confined field inside the particle. The classical bivector has a Lagrangian for the BFF, the first two terms, and another for the LFF, the last term, together giving

$$\mathcal{L}_{\text{BiSM}} = -\frac{1}{4} G_{\mu\nu} G^{\mu\nu} + \frac{1}{2} M^2 A_\mu A^\mu + g J^\mu A_\mu \tag{57}$$

following chapter 22 of [16]. In the quantum domain, the Dirac disc is in the BFF in correspondence with the classical BFF. The Weyl equation gives vector motion around the 2-axis in the LFF, see Appendix A. That means the two complementary classical spaces, LFF and BFF, undergo a continuous change until the space bifurcates into matter and force.

The parity of the BFF is even and that of the LFF is odd. The Lagrangian for the full Dirac equation is well known [1], and for the 2D equation, we write it using the even parity state, Ψ^+, Equation (22),

$$\mathcal{L}_{\text{2D Dirac}} = \bar{\Psi}^+ (i\gamma_s^0 \partial_0 + i\gamma_s^1 \partial_1 + i\gamma_s^3 \partial_3) \Psi^+ - M \bar{\Psi}^+ \Psi^+ \tag{58}$$

Using Equation (10), and likewise for the derivative $\partial_\pm = \frac{1}{\sqrt{2}}(\partial_3 \pm \partial_1)$, we suppress the subscript s on the derivatives, and transform it into the resonance basis:

$$\gamma_s^1 \partial_1 + \gamma_s^3 \partial_3 = \gamma_s^+ \partial_+ + \gamma_s^- \partial_- \tag{59}$$

From Figure 5 on the left, there are two cases of the orientation of the bivector in the external field: either within the interaction plane, 31, or outside that plane. The long arrows indicate the field polarization. Although Φ is fixed for a given configuration, the tandem precession of the two axes causes their projections to cycle through being in-phase along the bisector, e_{13}^+ (alignment), and out-of-phase along the horizontal, $\pm e_{13}^-$ (anti-alignment). This phase coherence arises from the relative precession phase, $\chi(t)$, Equation (37), not from a changing Φ.

Within the 31 plane, the spin remains coupled as spin-1, and this precesses about the field. There are two components, Equation (59). The former constructively interferes to give the resonant spin-1, while the latter destructively interferes and cancels. The fermion approximation drops the negative term leaving only a spin-1 resonant contribution. Likewise, outside the interaction plane, the leading blade interacts with the field. This reduces the Lagrangians to have spatial terms of

$$\begin{aligned} \left(\gamma_s^1 \partial_1 + \gamma_s^3 \partial_3\right) &\xrightarrow[\text{Fermion approximation}]{\text{Outside the 31 plane}} \gamma_s^i \partial_i \\ \left(\gamma_s^+ \partial_+ + \gamma_s^- \partial_-\right) &\xrightarrow[\text{Resonance approximation}]{\text{Inside the 31 plane}} \gamma_s^+ \partial_+ \end{aligned} \tag{60}$$

Then, the 2D Dirac equation in the presence of a field becomes

$$\left(i\gamma_s^0 \partial_0 + i\gamma_s^k \partial_k - M\right)\Psi^+ = 0 \tag{61}$$

as the case might be ($k = 1, 3, +$). This means that in a field at low, non-relativistic frequencies, spin becomes the usual spin up and down as commonly visualized and used.

There is a second Lagrangian for the Weyl equation, using the odd parity state, Ψ^- [4],

$$\mathcal{L}_{\text{Weyl}} = \frac{1}{2}\left(\Psi^{-\dagger} i\sigma^2 \partial_2 \Psi^- + \text{h.c.}\right) \tag{62}$$

This equation is in the LFF, with torque about the e_2 axis. Left or right precession gives the two helicity states, which are Hermitian conjugates. It is unlikely that there are benefits to quantizing the external torque.

7.2. Quantization

We regard structure as providing the geometric framework in which internal motions arise, giving physical properties that can be measured and visualized. The solution to Equation (61) in a polarizing field leads to a precessional cone of angular momentum at the Larmor frequency around the aligned axis. We have arrived at a real structure with internal motion. It is at this point that quantization is applied.

A useful comparison is the bonding structures of molecules, which are rigid under the Born–Oppenheimer approximation [86]. Within this structure, various quantized dynamics can be hosted. The philosophy follows that structure and function are related, and is consistent with the electron structure hosting its own energy, rather than being an excited state on a spacetime field.

We defined Planck's constant as the angular momentum of the spin-1 when $\Phi = 0$, from which we deduce each axis has angular momentum of $\pm\frac{h}{2}$. To reflect this, we retain

the physical condition that an integral number, m, of wavelengths fit around a cone with $m\lambda = 2\pi r$. We modify the de Broglie relation to have an angular momentum of $\frac{h}{2}$:

$$p = \frac{h}{2\lambda} \tag{63}$$

and the spin angular momentum becomes

$$\mathbf{S} = rp\,\hat{\mathbf{n}} = \frac{rh}{2\lambda}\,\hat{\mathbf{n}} \tag{64}$$

We assume the cone quantization, with radius r to give

$$\lambda = \frac{2\pi r}{m}, \quad \text{so that} \quad \mathbf{S} = m\frac{\hbar}{2} = \pm\frac{1}{2}\hbar \tag{65}$$

which are the two observed states depending on which axis is physically aligned. Therefore, the angular momentum magnitude in Equation (65) is $\frac{h}{2}$, and spin quantum numbers are $m = \pm 1$, which coincide with the blade assignments. This avoids half-integral quantum numbers, which are representations of fermions, not bosons. Nonetheless, it is convenient to treat fermion blades as having half-integer spin with $\hbar$ than integer spin with $\frac{\hbar}{2}$. This maintains integral quantization while assigning the correct angular momentum to the blade.

This also presents the possibility that the various generations, or flavors, of fermions are excited states of the quantized cones and not separate particles in the SM. However, we were unable to account for the mass differences of the leptons flavors using energy increase and special relativity alone [1,85,87,88].

7.3. No Superposition; No Collapse

In the BiSM, a spin state is a single-oriented plane, which is a unit bivector. Linear sums of such states generally leave the state space unless the planes coincide, so we cannot use vector–space superposition for bivector spins. Instead, spins are compared and combined only geometrically by alignment and rotation. Thus, a sum of bivectors is just an algebraic object, not a new spin state, in contrast to the vector–space sums and superposition used in the SM.

Therefore, the main ontological difference between the SM and the BiSM lies in the meaning of a state. In QM, the state of a physical system is completely described by a unit vector ψ called the state vector or wavefunction. It is defined in a complex Hilbert space and often expressed by a ket vector, $|\psi\rangle$. It has no physical meaning by itself and is mathematically a probability amplitude. Superposition must follow and is the principle that a system can exist in multiple possible states simultaneously. If $|\psi_1\rangle$ and $|\psi_2\rangle$ are valid quantum states, then so is any linear combination.

$$|\Psi\rangle = c_1|\psi_1\rangle + c_2|\psi_2\rangle \tag{66}$$

where c_1 and c_2 are complex coefficients. This structure of the Hilbert space enables interference, entanglement, and the Born rule. Measurement collapses the system into one of the basis states, with probabilities determined by the coefficients. Superposition of spin states is fundamental in QM.

In GA, states are not represented by abstract vectors in a Hilbert space but by real geometric entities in our 3D space. The fundamental operation in GA is the geometric product, which is linear and mixes different geometric grades. State evolution is described by rotor, R, transformations:

$$\rho' = R\rho R^{\dagger} \tag{67}$$

and measurement is modeled by geometric projection or alignment. Here, ρ is the state or density operator [89].

The Born rule emerges by expanding the wavefunction in the eigenbasis of an observable A:

$$A = \sum_i a_i |a_i\rangle\langle a_i| \tag{68}$$

The expectation value is given by

$$\begin{aligned}\langle A\rangle = \langle\psi|A|\psi\rangle &= \sum_i a_i |\langle a_i|\,\psi\rangle|^2 \\ &= \sum_i a_i P(a_i) \approx \left\langle RAR^\dagger \right\rangle_0\end{aligned} \tag{69}$$

in terms of the probability of measuring eigenvalue a_i. The Schrödinger equation determines the state, $|\psi\rangle$, from its Hamiltonian. The last equality is the expectation value in GA. The observable A is not given by Equation (68) but represents the state, usually a projection, of a structured object. In GA, that object is rotated by R to its new orientation, and the expectation value is defined as the scalar part of the multivector, $RAR^\dagger$. In QM, the expectation value is a statistical average computed from abstract wavefunctions. In geometric algebra, it is defined as the scalar part of the rotated observable, $\langle\cdot\rangle_0$, representing a direct geometric projection with no need for collapse [14].

There is an alternate way to express the state by using the density or state operator [28] where the expectation value is given by

$$\langle A\rangle = \mathrm{Tr}(\rho A) \tag{70}$$

using the quantum trace. The density operator is defined as the outer product of the wavefunction:

$$\rho = |\psi\rangle\langle\psi| \tag{71}$$

It is generally believed the wavefunctions and density operators give identical results, and they do if the SM Hamiltonian is used in both cases. For example, the usual state operator for a spin-$\frac{1}{2}$ is [89]

$$\rho = \frac{1}{2}(I + \mathbf{P}\cdot\sigma) \tag{72}$$

where $\mathbf{P}$ is the polarization. For a pure state, $\mathbf{P} = \hat{\mathbf{n}}$ where $\hat{\mathbf{n}}$ is a unit vector on the Bloch sphere. Spin is expressed as a Pauli operator, and the expectation values obtain using Equation (69) are

$$P_{Z,+} = \cos^2\left(\frac{\theta}{2}\right), \quad P_{Z,-} = \sin^2\left(\frac{\theta}{2}\right) \tag{73}$$

as usual [33]; in this case, the angle between $\hat{\mathbf{n}}$ and the measurement direction, Z, is θ.

In the BiSM, the complete bivector spin does not align with a field in favor of one axis, say e_3. Its partner, e_1, randomizes. From the BFF, that spin component, $\mathbf{S}_0 = e_3$, is rotated to the LFF using the rotation operator, R:

$$\mathbf{S} = Re_3R^\dagger \quad R = \exp\left(B\frac{\theta}{2}\right) \tag{74}$$

where the bivector is $B = e_1 \wedge e_2$. The measured spin component from the internal axis, e_3, is

$$\mathbf{S}\cdot e_3 = \cos\theta \tag{75}$$

thereby defining θ. Since $\cos\theta \in [-1, 1]$, we re-scale to obtain a "probability" in $[0, 1]$:

$$P_{Z,\pm} \equiv \Pi_{Z,\pm} = \frac{1 \pm \cos\theta}{2} \tag{76}$$

giving Equation (73). However, this result is not a probability in the BiSM but the definite orientation, Π, in 3D space. This does not depend upon quantization, but rather the axis that is closer to the field, **a**, will align, and its partner randomizes out (Equation (60)). This interpretation avoids superposition, collapse, and the Born rule. It instead derives outcome orientations from classical constructs: rotation, projection, and re-scaling. However, this is not a random process and is not a statistical ensemble of many events. We conclude that the two quantum spin states, expressed as vectors with symmetry SU(2), are entirely different in the BiSM. Those spin states of up and down are the two physical axes, 1 and 3, aligning with opposite chirality. That process is classical, not quantum. In contrast to the SM, the Pauli operators are not quantum but describe the two chiralities of a classical bivector.

A basic difference lies in the Lagrangians for a point and a bivector. Since calculating the state vector, $|\psi\rangle$, is avoided, we go directly to the state operator, ρ, and the Hamiltonian is defined by Equation (57):

$$H_{BiSM} = \frac{\partial \mathcal{L}_{\text{BiSM}}}{\partial \dot{q}_i} \dot{q}_i - \mathcal{L}_{\text{BiSM}} \tag{77}$$

Rather than the Schrödinger equation, the BiSM uses the von Neumann, or quantum Liouville, equation [28]:

$$i\hbar \frac{\partial \rho}{\partial t} = [H_{BiSM}, \rho]_- \tag{78}$$

Now, the two Hamiltonians are different, and Equations (69) and (70) give different results. If a physical bivector structure is reduced to a point, spatial derivatives vanish, eliminating internal energy terms. Thus, the spin Hamiltonian in the SM is a spatially degenerate case of the BiSM. None of the internal coherence, precession, or geometric structure is accessible.

7.4. The Fermion Approximation

The ontological differences between the SM and the BiSM are major. Some of the consequences are also far reaching, impacting quantum information theory [90], cosmology [91], and the foundations of physics [92]. Without Bell's theorem [5,6], non-locality and teleportation [93,94] are replaced by the correlation between bivectors and introduce spin quantum coherence as an element of reality [5]. Quantum computing must abandon teleportation and qubit superposition, which is the very motivation for the field [95]. Quantum computing would retain the classical binary processes, but an advantage may lie in using the deterministic chirality of electrons as quantum bits. Spin provides a stable deterministic way to predict binary outcomes by controlling the initial phase of the particle at the source and the field orientation at the filter.

Whereas the usual fermion of spin up and down is entrenched as a vector in a two dimensional Hilbert space, in the BiSM, all objects are oriented in physical space. Therefore, these objects are rotated in 3D space as seen in the last example. In studying the relation between structure and function, it is always easier to visualize in the BFF. Then, we simply transform to the LFF where measurements are carried out. We follow this approach.

Based upon Equation (31) and [4], the two axes are summed to give the resultant

$$\Sigma_{31} = \Sigma_3 + \Sigma_1 \tag{79}$$

After taking the expectation values in the BFF, this becomes pure geometry:

$$\langle \mathbf{\Sigma}_{31} \rangle = e^{+}_{13} + ie^{-}_{13}Y \approx e^{+}_{13} = \frac{1}{\sqrt{2}}(e_3 + e_1) \tag{80}$$

We used the resonance approximation (Equation (60)). In the presence of a field, **a**, and within the interaction plane, 31, the spin-1 precesses around the bisector, e^{+}_{31}. The last term shows the interactions with the field, giving

$$\mathbf{a} \cdot \langle \Sigma_{31} \rangle = \frac{1}{\sqrt{2}}\mathbf{a} \cdot (e_3 + e_1) \tag{81}$$

The projections from each axis in the LFF are

$$\begin{aligned} \mathbf{a} \cdot e_3 &= \cos(\theta_a - \theta) \\ \mathbf{a} \cdot e_1 &= \sin(\theta_a - \theta) \end{aligned} \tag{82}$$

and there is a competition in Equation (81). Since the axes are rigidly orthogonal, only one can align. Based on Least Action, we take the larger magnitude between the cosine and sine as the indicator as to which is closer to the field, **a**. That axis aligns, and its partner averages out. Such interactions are well known and widely used [96]. The angle θ is set at the source, and since both θ_a and θ angles can be controlled in experiment, the alignment of axes is deterministic.

In mainstream physics and chemistry, QM is applied to spectroscopies and quantum physics with great success. All such studies involve particles in a field where the spin is polarized. When one axis is aligned, which is the usual case, the resulting particle has all the properties of a fermion. It is still, however, a bivector and cannot superpose, but vectors in physical space can add. Therefore, under polarized conditions, treating the bivector as an effective fermion maintains the successful spectroscopic techniques involving angular momentum addition, couplings, energy levels, transition intensities, and shifts. The Clebsch–Gordan algebra applies unchanged [97]. Both the Wigner–Eckart Theorem and the Golden Rule remain valid but only under SO(3) symmetry, not SU(2). That is, the RHS of Figure 7 is used. With that restriction, only the six blades of spin-1 and -2 are retained, and they are chiral vectors. The fermion approximation, Equation (60), treats a polarized blade as a fermion but without superposition.

8. SM—BiSM and Experiment

8.1. The "Origin of Positrons in the Galaxy" Puzzle

Despite the widespread acceptance of electron–positron annihilation as a cornerstone of Dirac's theory, direct astrophysical evidence for widespread pair annihilation in the cosmos is scant [98]. Each photon produced in electron–positron annihilation has rest mass of 511 keV. Only narrow 511 keV gamma-ray lines have been observed [99], and their origin remains unclear and do not constitute definitive proof of ubiquitous electron–positron annihilation. Expected large-scale annihilation signatures in the interstellar medium or from early-universe pair production events are absent [100]. This challenges the notion that the positron is a true physical antiparticle of the electron as postulated in the Dirac spinor formalism. The lack of observational support for universal annihilation phenomena, therefore, favors the BiSM that does not rely on the existence of fundamental particle–antiparticle pairs.

8.2. Separating Vector and Bivector Motion

EPR coincidence experiment, [33–35], that show violation of Bell's Inequalities, are used to confirm that Nature is not locally real. Figure 4, however, shows the violation arises from correlation between vectors and between bivectors. In the experiments, from a random source, these combine using the Minkowski sum, to give the apparent violation of Bell's Inequalities. It should be possible to separate the vector from bivector correlation.

Using Equation (82) shows that if the initial orientation at the source, θ, lies within $\frac{\pi}{4}$ of the fields of both Alice and Bob, (within their common interaction planes) then the coincidences are dominated by bivector correlation, [6]. If θ lies beyond $\frac{\pi}{4}$, (so out of their interaction plane), then the vector correlation dominates. This technique should separate the two, and give deterministic outcomes which can act as true quantum bits.

8.3. Low-Energy Studies

The above constitute low-energy experiments. More generally, if the BiSM electron is viable, then we should be able to control the processes and use chirality of the electron, which carries the left and right hands of Nature.

Advances in low-energy photon experiments, such as those above by [33–35] and methods discussed by Steinberg [101], provide the appropriate platform for exploring deterministic models of spin alignment without shattering bivectors into their chiral bits as the LHC does. As above, we propose photon experiments using low-energy laser sources, allowing the experimenter to actively set the initial phase angle θ at the source within the disc plane. The relative phase $(\theta_a - \theta)$ determines the spin projection based on the larger component aligning as spin "up" or spin "down". Control of the source phase and field orientation should be consistent with deterministic outcomes of spin alignment without invoking probabilistic collapse.

The question arises as to how Nature controls its bosons to create structures, quark confinement, and so on up to bonding and molecular formation. One may be encouraged by advances in chemistry and biochemistry involving self-assembly where, primarily, the experimenter provides the ingredients and controls the environment. Self-assembly is the autonomous organization of components into patterns or structures without human intervention [102].

8.4. Classical Bivector

We did not find any classical experiments that study a spinning bivector. Consider spin as an angular momentum engine. The system receives an input torque about the e_2 axis, corresponding to the drive shaft. The wedge $e_1 \wedge e_3$ represents the internal working of the engine, with the two counter-precessing axes absorbing and storing torque as rotational kinetic energy. The external LFF reveals measurable quantities such as spin projection, torque, the zbw, and the precession behavior. Building and treating a classical spin as a mechanical engine allows engineering techniques to be applied, from torque analysis to calorific measurements.

Such a rigid apparatus has two perpendicular rods representing the bivector axes with, perhaps, magnetic tips on e_1 and e_3 and mounted to spin freely in its own plane while being precessed about the shaft. One goal is to detect the growth of a magnetic vector along the bivector bisector, 13. LEDs or reflective markers attached along the rods would not detect the classical spin but would allow for the motion to be followed using high-speed cameras or long-exposure imaging. To detect magnetic effects, the detector must be stationary at the origin of the BFF and directed along the bisector.

NV (nitrogen-vacancy) center magnetometers [103,104] can be integrated into small, solid-state structures embedded in diamond chips, making them candidates for mounting

directly into the spinning system. These devices are capable of detecting vector magnetic fields. Their output can be transmitted optically. When illuminated by green laser light, the NV center fluoresces in the red. They detect local magnetic fields with spatial resolution down to the nanoscale. NV centers are solid-state and operate at room temperature and easily embedded into the BFF where traditional magnetometers would be impractical. If a resonance spin was detected, placing it in a magnetic field might reorient the resonance as we describe here.

The presence of even a small magnetic component along the 13 axis would confirm the spin-1 character of the bivector and that spin has a classical origin. Such an experiment might also confirm the zbw [17], which has its possible source in the Compton scale internal precession (Equation (35)).

8.5. The Muon g-2 Anomaly

The muon anomalous magnetic moment $a_\mu = (g-2)/2$ reveals a significant discrepancy between experimental results and the SM prediction. Recent measurements at Fermilab [105] report a value of

$$a_\mu^{\text{exp}} = 116592061(41) \times 10^{-11} \tag{83}$$

while SM calculations yield

$$a_\mu^{\text{SM}} = 116591810(43) \times 10^{-11} \tag{84}$$

leading to a deviation of approximately 4.2σ to 5σ.

In the BiSM, the muon is modeled as a spin-1 bivector rather than a point particle. Its internal rotor structure gives rise to spin-$\frac{1}{2}$ projections. Shifts in the precessional geometry or coherence between internal blades, again seen in Equation (37), can be modulated by mass or field interactions. These shifts may result in observable deviations from the Dirac prediction. Such geometric effects may offer a classical explanation for the $g-2$ anomaly without invoking loop corrections [106], which successfully measure quantum fluctuations, or supersymmetric particles [107], which have never been observed. Thus, the muon anomaly may serve as experimental evidence for the bivector structure.

8.6. Electron Quadrupole Moment

The SM predicts an electron has no quadrupole moment, whereas the BiSM predicts a very small quadrupole. To date, high–precision experiments [108,109] have not detected it. The reason the SM has no quadrupole is due to the matrix element being zero [81]

$$\langle \tfrac{1}{2}, m \mid Q_{ij} \mid \tfrac{1}{2}, m' \rangle = 0 \tag{85}$$

where the electric quadrupole operator, Q_{ij}, has nonzero matrix elements only for total spin ≥ 2.

In BiSM, the electron is a finite-sized rotor with radius, R, assumed proportional to the Compton wavelength [110]:

$$R \equiv \eta \lambda_C, \qquad \lambda_C = \frac{\hbar}{m_e c} \approx 3.86 \times 10^{-13}\,\text{m} \tag{86}$$

so that if its charge is distributed uniformly on the thin disc of the interaction plane, 13, the classical electric quadrupole moment is

$$Q_e = \int d^3r\, \rho(\mathbf{r})\left(3z^2 - r^2\right) \approx \frac{e\,R^2}{2} = \frac{e}{2}\left(\eta\,\lambda_C\right)^2 \tag{87}$$

$$\sim 5 \times 10^{-46}\,\mathrm{C}\cdot\mathrm{m}^2 \tag{88}$$

The value $\eta \approx 0.06$ is estimated from the rim velocity. From classical mechanics, using $S = I\omega$ with the moment of inertia $I = m_e R^2$ and intrinsic spin $S = \frac{\hbar}{2}$, we obtain

$$\omega = \frac{\hbar}{2m_e R^2} \tag{89}$$

giving

$$v_{\mathrm{rim}} = \omega R = \frac{\hbar}{2m_e \eta \lambda_C} = \frac{c\cdot\eta}{2} \tag{90}$$

with $v_{\mathrm{rim}} = 0.03c$, Equation (15), and $\eta = 0.06c$.

This quadrupole gives a shift in the energy of the hydrogen 1s state of

$$\Delta E \simeq -\frac{Q_e}{20\pi\varepsilon_0\, a_0^3} \sim 10^{-21}\,\mathrm{eV}. \tag{91}$$

Penning-trap and atomic-clock experiments [108,109] cannot yet detect such a small shift by several orders of magnitude, but detecting a nonzero ΔE would provide compelling evidence for the BiSM.

8.7. Problems with Chirality

The classical treatment of spin needs to be related to other work. The BMV equation [111–113] describes spin in EM fields and is widely used. Foldy and Wouthuysen [114–116] provide a non-relativistic reduction of the Dirac equation for spin-$\frac{1}{2}$. Although BiSM replaces spinors by bivectors, these treatment address classical phenomena that the BiSM should reproduce. There is also need for more detailed recalculations of experimental observables, such as the beta spectra [117]. However, such tasks require the development of new modeling based upon BiSM. Our aim is not to produce a full replacement for the SM's computational machinery but rather to establish the physical and geometric foundations that motivate such development within the BiSM. To that end, we have identified points of departure from the SM and see this work as laying the groundwork and theoretical basis for future studies. Detailed numerical modeling lies beyond the scope of the present paper.

In Table 1, some approaches to spin formulation are compared. The SM is theoretically sound and experimentally accurate. It is considered a success of theoretical physics. Many predictions are confirmed to high precision [118,119]. These are cited as validating the gauge theory approach and gives a mathematical framework for particle interactions. These successes are primarily for non-chiral particles. The electron g-factor and muon g-2 calculations do not depend upon chirality [120], neither do the successful explanation of the Lamb shift [121] and the Casimir effect [122] that depend upon vacuum fluctuations. These and other successes of the SM need to be examined in the BiSM and are likely to be equally successful with different perspectives.

Table 1. Comparison of BiSM with other major frameworks for spin and the Dirac equation.

Framework	Approach	Strengths	Weaknesses
Bivector SM	The bivector boson spin-1 is fundamental in $Cl(2,2)$, and fermions are its blades; classical mechanics and geometric algebra; defines the quantum state as parity +1.	Ontic; unifies bosons-fermions; classical-quantum correspondence; mass, charge, and spin emerge; clarifies parity; origin of the double helix; parity conserved in β-decay; neutrinos not needed; no superposition and collapse; local; disproves Bell's theorem.	Highly nonstandard; requires vast reinterpretation SM data; untested.
Standard Model [1]	Gauge-theoretic QFT with fermions as fundamental; bosons arise from gauge fields; uses SU(3)$\times$ SU(2)$\times$U(1).	Matches much of the high-energy experimental data; predictive; deeply integrated into QFT and particle physics.	Relies on unexplained parameters; parity violation; no ontic spin; non-local; chirality issues; semantically confusing; mathematically dense.
Hestenes [13,14]	Uses GA; spinors as real even multivectors in $Cl(1,3)$; keeps fermions as fundamental.	Geometric clarity; keeps full QM predictive power; clarifies zbw and spin.	Retains superposition and fermions; does not change SM ontology; rests within QM formalism.
Doran and Lasenby [7]	General spacetime algebra (STA) framework $Cl(1,3)$ for fields; rotor formalism for spin; unifies GA treatment of relativity and QM.	General; powerful for both relativity and QM in unified formalism; widely cited.	Retains SM ontology and quantum postulates; retains superposition.
Twistor Theory [123,124]	Formulates spacetime and fields in complex projective space; spinors are fundamental; aims at unifying geometry with quantum theory.	Related to conformal geometry and spin; applied to scattering amplitudes. Simplifies Feynman diagrams. Developed the Penrose transform.	Abstract, highly mathematical; physical interpretation less direct; built on spinor ontology.

The SM's conceptual difficulties appear to primarily involve chirality, parity violation, and flavor structure. These are expressed [125] with the conclusion that we must go beyond the SM, i.e., BSM. The BiSM resolves many of these issues, not by going beyond but by replacing the SM with a simpler and physical framework. Generally, we conclude that the mathematical basis of the SM permits the proliferation of particles and ad hoc corrections. In contrast, visualization of the geometric structures of the BiSM constrains concepts that are mathematically viable.

The BiSM is a new approach and has not been experimentally tested. However, it provides a clear framework by which observable vector quantities arise from internal bivector coherence. In cases that we have studied, except for neutrinos, the experimental data are not violated, only re-interpreted.

9. Summary

In QM, superposition arises from treating the state of a spin-$\frac{1}{2}$ particle as a vector in a Hilbert space, where any linear combination of basis spinors, Equation (66), also represents a valid state. This abstract linearity leads to probabilistic collapse and entanglement, but

without a tangible geometric interpretation. In contrast, the bivector spin model does not describe states as vectors in an abstract space but as real geometric objects like we experience. A bivector is a structured entity, not a linear combination of states. When a bivector spin is defined, Equation (11), that spin state is completely determined and visualized by an oriented bivector plane with a left and right hand, and a double helix of properties. The binary symmetry of Nature that surrounds us cannot be a coincidence.

An electron is the likely the smallest engine in Nature, delivering mass, energy and force to a target to deterministically build matter. Just as engineers rotate and project from their machine to extract values and data, so Nature does the same. The BiSM follows this protocol, but the SM does not, allowing for a pool of non-deterministic and probabilistic states.

Werner Heisenberg [126] reflected on the limits of interpreting the quantum world. He contrasted the German terms *Anschaulich* (intuitive or visual) and *Anschaulichkeit* (visualizability) to stress that, at microscopic scales, classical imagery breaks down, and we must rely on the equations. In the BiSM, we retain Heisenberg's concept but overturn his conclusion: classical visualization is not lost, but is evident through the geometry of structures. Rather than abandoning physical intuition, we recover it, being able to visualize processes that involve mass-energy, charge, spin, parity, *etc*.

Heisenberg's observation, however, underscores that the formulation of QM and the SM lacks the clarity of visualization and geometry. This is at odds with the basic goal of science which is to understand Nature with as simple an ontology as possible, but without sacrificing its predictive and empirical success. Einstein said, [127], "It can scarcely be denied that the supreme goal of all theory is to make the irreducible basic elements as simple and as few as possible, without having to surrender the adequate representation of a single datum of experience".

Isaac Newton said in his First Rule of Reasoning from the Principia, [128] "no more causes of natural things should be admitted than are both true and sufficient to explain their phenomena". He went on to say, "Nature does nothing in vain, and more causes are in vain when fewer will suffice. For Nature is simple and does not indulge in the luxury of superfluous causes".

We contend that, relative to the BiSM, the SM lacks ontological transparency and the BiSM gives deeper insight. The SM is conceptually opaque, and is non-parsimonious. It relies on a product of gauge groups, SU(3), SU(2) and U(1); representations are often ad hoc; independent tunable parameters which are fixed by experiment are added; and anomaly cancellation is introduced algebraically rather than arising from physically motivated mechanisms. In short, the SM explains by accretion.

Structure constrains mathematics. This, however, is not the philosophy of the SM. Without real geometry, formal methods like Feynman diagrams and gauge algebras, [1], become nonphysical, and lack a counterpart in Nature. Moreover, the difference between the mathematics of the two models is stark. The chiral fields of spinors that span all of spacetime only work because they are forced to cancels all gauge anomalies. They are purely mathematical processes and mostly physically obscure, like how the Higgs's field imparts mass. No gauge bosons have ever been observed, they exist off-shell, and mostly absorb recoil to restore symmetry. In comparison, the Geometric Algebra of the BiSM is mathematically straightforward and physically constrained. Two equations govern the bivector spin, Equations (11) and (13). The BiSM has states that are constructed from internally consistent geometries. Much of the confusion in the foundations [129], is eliminated in the BiSM, with no collapse or superposition to contend with.

Since superposition is rarely used in applications of QM to chemistry and physics, the only real change there is ontological. The changes occur at the foundational level:

particle physics, quantum information, neutrino science, CPT symmetries, and cosmology, which follow from the SM. There are two distinct ways to linearize the KG equation. Dirac introduced one such, which has become foundational to relativistic quantum theory. However, the discovery of a second linearization inspires comparison. Since both cannot simultaneously describe the same underlying structure, it is important to examine which formulation more accurately reflects physical reality. Despite the ontological simplicity of the BiSM, its predictive accuracy has not been developed, whereas the successes of the SM are well known.

This geometric reformulation has far-reaching implications. It avoids divergences and renormalization; bypasses negative energy solutions; resolves baryogenesis; and challenges the semantic overreach of the SM. Bell's inequalities apply only to a single convex set, and his theorem is disproven. Teleportation [94], returns to science fiction. The Wu data is re-interpreted showing parity is not violated in the weak force, and neutrinos are not needed in beta decay [75,76]. The BiSM rejects the definition of qubits as superposed fermions. These are replaced by the left and right hands of Nature, whereby the experimenters choice of helicity determines the chirality of the measured blade. Changing helicity has the effect of going from building structures (an asymmetrical Fermi-Dirac process), to applying force, (a symmetrical Bose-Einstein process). How, one may ask, can microscopic structures be built from a mechanics of the quantum domain that is random, non-deterministic, non-local, not real, and postulated with no geometrical basis? The BiSM shows that Nature is deterministic, local, and real, from which structures can naturally be built. Spin need not be postulated; energy and angular momentum remain conserved between the classical and quantum domains; parity quantization occurs at $\Phi = 0$, when the internal space of the bivector undergoes bifurcation of reflection into parity. Quantum spin, therefore QM, has a classical origin.

Funding: This research received no external funding.

Data Availability Statement: No new data were created or analyzed in this study. Data sharing is not applicable to this article.

Conflicts of Interest: The author declares no conflicts of interest.

Appendix A. Quantum Correspondence

For completeness, we summarize the QFT treatment of a quantum bivector to show the classical treatment is faithfully followed by the quantum. The details are given in reference [4] where the derivation from the KG equation is presented, showing isomorphism to the standard Clifford algebra, Cl(1,3), the change to Cl(2,2), and its metric signature and basis. Figure A1 illustrates this. The usual Dirac equation, top panel, obeys the Clifford algebra of Minkowski space, $Cl(1,3)$, with three spatial components and one time. Introducing the bivector renders the Dirac equation non-Hermitian, with $Cl(2,2)$: two time components (linear and helical period) and two spatial axes forming a disc. Its two solutions are the mirror states $\psi^{\pm}$, Equation (20), which are complex conjugates and denote opposite chirality. Under parity, the non-Hermiticity separates into two complementary equations: a two-dimensional Dirac equation describing the even-parity disc and a massless Weyl equation of odd parity describing helicity as a quaternion [4]. This approach is consistent with Twistor Theory [123,124], which complexifies Minkowski space by replacing the four real parameters with complex forms. Twistor space, T, is projected into two helicity spaces, $P^{\pm}T = T^{\pm}$. Here, we take the Dirac field D, complexify it to D_s, and then use $P_{13}D_s = (\gamma_s^0, \gamma_s^1, \pm\tilde{\gamma}_s^2, \gamma_s^3)$ to project out the two helicity states [4,5].

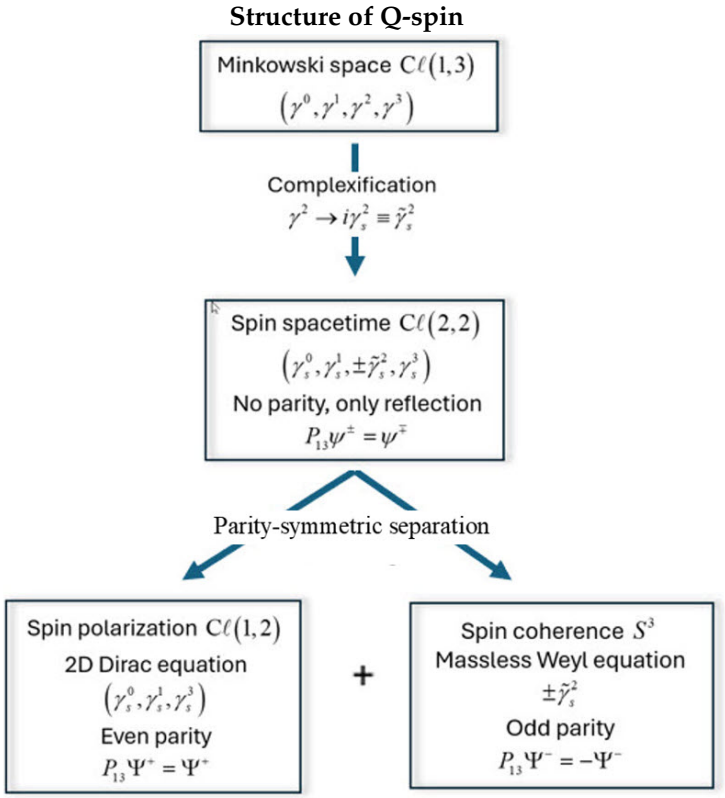

Figure A1. The structure and separation of spin spacetime into complementary spaces of polarization and coherent helicity.

Appendix B. Parentage Schemes

In Figure 7 [77–80], we distinguish between two parentage schemes: the Lie algebra scheme, which yields both half-integer and integer spin states, and the Cartesian approach, which produces only integer-spin states. The SM, based on spinors, is compared with the BiSM, which uses bivectors as fundamental.

On the left of Figure 7, the Lie algebra scheme follows angular momentum coupling rules to build higher-order spin states. Here, the order o denotes the number of spin-$\frac{1}{2}$ particles being coupled, and the weight w denotes the total spin resulting from these couplings. Successive coupling of spin-$\frac{1}{2}$ particles generates both half-integer and integer spin states. At each horizontal step to the right, a new spin-$\frac{1}{2}$ particle is added, and the total spin increases or decreases by $\frac{1}{2}$, forming a branching structure governed by Clebsch–Gordan rules [97]. The total number of components for each order is $n = 2^o$, corresponding to the full dimension of the spinor tensor product space. The multiplicity at each node indicates the number of distinct ways a given total spin can be formed through allowed pairwise couplings. The top diagonal ($w = o/2$) consists of totally symmetric combinations of spinors, forming the unique spin-$o/2$ irreducible representation of SU(2).

On the right side of the figure, the scheme is built not from spinors but from real vectors in $\mathbb{R}^3$. These vectors combine through inner products, cross products, and outer (symmetric traceless tensor) products. Each vertical column represents the full decomposition of the tensor product space into tensors of rank 0, 1, 2, and higher integer components. There are no spinors. The top diagonal ($w = o$) consists of symmetric traceless tensors, forming the unique irreducible representations of SO(3) [80].

Appendix C. Symmetry of Quaternion Spin

The standard Dirac equation represents spin through complex four-component spinors, invoking the symmetry group SU(2)⊗SU(2). Their spinor components $(\pm I, \pm\sigma_1, \pm\sigma_2, \pm\sigma_3)$;

have opposite chiralities; are mirror images under usual parity; and are interpreted as a matter–antimatter pair.

The anti-commutation relations are satisfied by quaternion gamma matrices, $\tilde{\gamma}_s^{\mu}$, which are also constructed using skew-diagonal Pauli components. These are real matrices, $(\pm I, \pm\sigma_1, \pm i\sigma_2, \pm\sigma_3)$, and their algebra forms the discrete quaternion group Q_8, which is isomorphic to the continuous group of unit quaternions, $\mathbb{H}$, under multiplication [130–132]. In the BiSM, spinor algebra is replaced by quaternionic geometry.

In analogy with the Dirac case, the SU(2) symmetry is replaced by the real algebra SL(2, $\mathbb{R}$), defined as the group of 2×2 real matrices with determinant $+1$. The full symmetry structure is then $\mathrm{SL}(2,\mathbb{R}) \otimes \mathrm{SL}(2,\mathbb{R})$, where each matrix represents one of the two orthogonal planes associated with each blade. This replaces the chiral spinor components in the SM with geometric planes with definite internal dynamics in the BiSM.

References

1. Peskin, M.; Schroeder, D.V. *An Introduction To Quantum Field Theory*; Frontiers in Physics: Boulder, CO, USA, 1995.
2. Dirac, P.A.M. The quantum theory of the electron. *Proc. R. Soc. Lond. Ser. A Contain. Pap. A Math. Phys. Character* **1928**, *117*, 610–624.
3. For a Pedagogical Survey. Available online: https://youtu.be/90W3aUl0gHU?si=uqtIU1mMNvdQJUzg (accessed on 21 August 2025).
4. Sanctuary, B. Quaternion Spin. *Mathematics* **2024**, *12*, 1962. [CrossRef]
5. Sanctuary, B. Spin Helicity and the Disproof of Bell's Theorem. *Quantum Rep.* **2024**, *6*, 436–441. [CrossRef]
6. Sanctuary, B. EPR Correlations Using Quaternion Spin. *Quantum Rep.* **2024**, *6*, 409–425. [CrossRef]
7. Doran, C.; Lasenby, J. *Geometric Algebra for Physicists*; Cambridge University Press: Cambridge, UK, 2003.
8. Dirac, P.A.M. A Theory of Electrons and Protons. *Proc. R. Soc. Lond. A* **1930**, *126*, 360–365.
9. Greiner, W. *Relativistic QM-Wave Equations*; Springer: Berlin/Heidelberg, Germany, 2000; pp. 310–360.
10. Paganini, P. *Fundamentals of Particle Physics: Understanding the Standard Model*; Cambridge University Press: Cambridge, UK, 2023.
11. Skyrme, T.H.R. A unified field theory of mesons and baryons. *Nucl. Phys.* **1962**, *31*, 556–569. [CrossRef]
12. Pezzaglia, W.M. Physical applications of a generalized Clifford calculus (Papapetrou equations and metamorphic curvature). *arXiv* **1997**, arXiv:gr-qc/9710027. [CrossRef]
13. Hestenes, D. Spin and uncertainty in the interpretation of quantum mechanics. *Am. J. Phys.* **1979**, *47*, 399–415. [CrossRef]
14. Hestenes, D.; Sobczyk, G. *Clifford Algebra to Geometric Calculus: A Unified Language for Mathematics and Physics*; Springer Science and Business Media: Berlin/Heidelberg, Germany, 2012; Volume 5.
15. Nash, C.; Sen, S. *Topology and Geometry for Physicists*; Elsevier: Amsterdam, The Netherlands, 1988.
16. Schwarz, A.S. *Quantum Field Theory and Topology*; Springer Science and Business Media: Berlin/Heidelberg, Germany, 2013; Volume 307.
17. Hestenes, D. The zitterbewegung interpretation of quantum mechanics. *Found. Phys.* **1990**, *20*, 1213–1232. [CrossRef]
18. Muralidhar, K. The spin bivector and zeropoint energy in geometric algebra. *Adv. Studies Theor. Phys.* **2012**, *6*, 675–686.
19. Goldstein, H. *Classical Mechanics*; Pearson Education India: Noida, India, 2011.
20. Nadler, E.O.; Benson, A.J. Semianalytic model for decaying dark matter halos. *arXiv* **2025**, arXiv:2501.12636. [CrossRef]
21. Carroll, S.M. *Spacetime and Geometry*; Cambridge University Press: Cambridge, UK, 2019
22. Leonard, I.E.; Lewis, J.E. *Geometry of Convex Sets*; John Wiley and Sons: Hoboken, NJ, USA, 2015.
23. Hadwiger, H. Minkowskische addition und subtraktion beliebiger punktmengen und die theoreme von erhard schmidt. *Math. Z.* **1950**, *53*, 210–218. [CrossRef]
24. Noether, E. Invariante Variations probleme. *Gott. Nachr.* **1918**, 235–257.
25. Etingof, P.; Golberg, O.; Hensel, S.; Liu, T.; Schwendner, A.; Vaintrob, D.; Yudovina, E. Introduction to representation theory. *arXiv* **2009**, arXiv:0901.0827
26. Ballentine, L.E. The statistical interpretation of quantum mechanics. *Rev. Mod. Phys.* **1970**, *42*, 358. [CrossRef]
27. Dirac, P. A.M. On the theory of quantum mechanics. *Proc. R. Soc. London A* **1926**, *112*, 661–677.
28. Von Neumann, J. *Mathematical Foundations of Quantum Mechanics*; Princeton University Press: Princeton, NJ, USA, 1955.
29. Aharonov, Y.; Susskind, L. Charge Superselection Rule. *Phys. Rev.* **1967**, *155*, 1428. [CrossRef]
30. Giacomini, F.; Castro-Ruiz, E.; Brukner, Č. Quantum mechanics and the covariance of physical laws in quantum reference frames. *Nat. Commun.* **2019**, *10*, 494. [CrossRef]
31. Bartlett, S.D.; Rudolph, T.; Spekkens, R.W. Reference frames, superselection rules, and quantum information. *Rev. Mod. Phys.* **2007**, *79*, 555. [CrossRef]

32. Bell, J.S. On the Einstein Podolsky Rosen paradox. *Phys. Phys. Fiz.* **1964**, *1*, 195. [CrossRef]
33. Clauser, J.F.; Horne, M.A.; Shimony, A.; Holt, R.A. Proposed experiment to test local hidden-variable theories. *Phys. Rev. Lett.* **1969**, *23*, 880. [CrossRef]
34. Aspect, A.; Dalibard, J.; Roger, G. Experimental test of Bell's inequalities using time-varying analyzers. *Phys. Rev. Lett.* **1982**, *49*, 1804. [CrossRef]
35. Weihs, G.; Jennewein, T.; Simon, C.; Weinfurter, H.; Zeilinger, A. Violation of Bell's inequality under strict Einstein locality conditions. *Phys. Rev. Lett.* **1998**, *81*, 5039. [CrossRef]
36. Bell, J.S. *Speakable and Unspeakable in Quantum Mechanics*; Cambridge University Press: New York, NY, USA, 1987; p. 65.
37. Brunner, N.; Cavalcanti, D.; Pironio, S.; Scarani, V.; Wehner, S. Bell nonlocality. *Rev. Mod. Phys.* **2014**, *86*, 419–478. [CrossRef]
38. Wiseman, H.M. The two Bell's theorems of John Bell. *J. Phys. A Math. Theor.* **2014**, *47*, 424001. [CrossRef]
39. Kupczynski, M. Quantum nonlocality: How does nature do it? *Entropy* **2024**, *26*, 191. [CrossRef] [PubMed]
40. Kochen, S.; Specker, E.P. The problem of HV in quantum mechanics. In *Ernst Specker Selecta*; Birkhäuser: Basel, Switzerland, 1990; pp. 235–263.
41. Schwinger, J. Quantum electrodynamics. I. A covariant formulation. *Phys. Rev.* **1948**, *74*, 1439. [CrossRef]
42. Feynman, R.P. Space-time approach to quantum electrodynamics. In *Quantum Electrodynamics*; CRC Press: Boca Raton, FL, USA, 2018; pp. 178–198
43. Dyson, F.J. The Radiation Theories of Tomonaga, Schwinger, and Feynman. *Phys. Rev.* **1949**, *75*, 486 [CrossRef]
44. Gell-Mann, M.; Low, F.E. Quantum electrodynamics at small distances. *Phys. Rev.* **1954**, *95*, 1300. [CrossRef]
45. Wilson, K.G. Renormalization group and critical phenomena. I. Renormalization group and the Kadanoff scaling picture. *Phys. Rev. B* **1971**, *4*, 3174. [CrossRef]
46. Wilson, K.G.; Kogut, J. The renormalization group and the epsilon expansion. *Phys. Rep.* **1974**, *12*, 75–199. [CrossRef]
47. Gross, D.J. Twenty five years of asymptotic freedom. *Nucl. Phys. B-Proc. Suppl.* **1999**, *74*, 426–446 [CrossRef]
48. Sanyuk, V.I.; Sukhanov, A.D. Dirac in 20th century physics: A centenary assessment. *Phys.-Uspekhi* **2003**, *46*, 937. [CrossRef]
49. Wilczek, F. Quantum mechanics of fractional-spin particles. *Phys. Rev. Lett.* **1982**, *49*, 957. [CrossRef]
50. Kamada, S. *Braid and Knot Theory in Dimension Four*; American Mathematical Socient: Providence, RI, USA, 1964.
51. Charvin, G.; Vologodskii, A.; Bensimon, D.; Croquette, V. Braiding DNA: Experiments, simulations, and models. *Biophys. J.* **2005**, *88*, 4124–4136. [CrossRef] [PubMed]
52. Khrennikov, A. Contextual approach to quantum mechanics and the theory of the fundamental prespace. *arXiv* **2003**, arXiv:quant-ph/0306003. [CrossRef]
53. Khrennikov, A.Y. *Contextual Approach to Quantum Formalism*; Springer Science & Business Media: Berlin/Heidelberg, Germany, 2009; Volume 160.
54. Gell-Mann, M. The Interpretation of the New Particles as Displaced Charged Multiplets. *Nuovo C.* **1956**, *4* (Suppl. S2), 848–866. [CrossRef]
55. Nakano, T.; Nishijima, N. Charge Independence for V-particles. *Prog. Theor. Phys.* **1953**, *10*, 581 [CrossRef]
56. Griffiths, D. *Introduction to Elementary Particles*; Wiley: Hoboken, NJ, USA, 2009; pp. 59–60, ISBN 978-3-527-40601-2.
57. Laurikainen, K.V. *Beyond the Atom: The Philosophical Thought of Wolfgang Pauli*; Springer Science & Business Media: Berlin/Heidelberg, Germany, 2012.
58. Pauli, W. Pauli Letter Collection: Letter to Lise Meitner (No. CERN-ARCH-PLC, pp. Letter-2412). 1930. Available online: https://cds.cern.ch/record/83292?ln=en (accessed on 21 August 2025).
59. Fermi, E. Versuch einer Theorie der β-Strahlen. I. *Z. FüR Phys.* **1934**, *88*, 161–177. [CrossRef]
60. Fukuda, S.; Fukuda, Y.; Hayakawa, T.; Ichihara, E.; Ishitsuka, M.; Itow, Y.; Kajita, T.; Kameda, J.; Kaneyuki, K.; Kasuga, S.; et al. The super-kamiokande detector. *Nucl. Instrum. Methods Phys. Res. Sect. A Accel. Spectromet. Detect. Assoc. Equip.* **2003**, *501*, 418–462. [CrossRef]
61. Abbasi, R.; Ackermann, M.; Adams, J.; Ahlers, M.; Ahrens, J.; Andeen, K.; Auffenberg, J.; Bai, X.; Baker, M.; Barwick, S.; et al. The IceCube data acquisition system: Signal capture, digitization, and timestamping. *Nucl. Instrum. Methods Phys. Res. Sect. A Accel. Spectromet. Detect. Assoc. Equip.* **2009**, *601*, 294–316. [CrossRef]
62. Bellerive, A.; Klein, J.R.; McDonald, A.B.; Noble, A.J.; Poon, A.W. The Sudbury Neutrino Observatory. *Nucl. Phys. B* **2016**. [CrossRef]
63. Waxman, E. Neutrino astrophysics: A new tool for exploring the universe. *Science* **2007**, *315*, 63–65. [CrossRef]
64. Mertens, S. Direct neutrino mass experiments. *J. Phys. Conf. Ser.* **2016**, *718*, 022013. [CrossRef]
65. Abe, S.; Ebihara, T.; Enomoto, S.; Furuno, K.; Gando, Y.; Ichimura, K.; Ikeda, H.; Inoue, K.; Kibe, Y.; Kishimoto, Y.; et al. KamLAND Measurement of Reactor Antineutrino Disappearance in the First Phase of the KamLAND Experiment. *Phys. Rev. Lett.* **2008**, *100*, 221803. [CrossRef]
66. An F.P.; Bai, J.Z.; Balantekin, A.B.; Band, H.R.; Beavis, D.; Beriguete, W.; Bishai, M.; Blyth, S.; Boddy, K.; Brown, R.L.; et al. Observation of electron-antineutrino disappearance at Daya Bay. *Phys. Rev. Lett.* **2016**, *108*, 171803. [CrossRef]

67. Bellini, G.; Benziger, J.; Bick, D.; Bonfini, G.; Bravo, D.; Avanzini, M.B.; Caccianiga, B.; Cadonati, L.; Calaprice, F.; Carraro, C.; et al. Cosmic-muon flux and annual modulation in Borexino at 3800 m water-equivalent depth. J. Cosmol. *Astropart. Phys.* **2012**, *2012*, 015. [CrossRef]
68. Aartsen, M.G.; Ackermann, M.; Adams, J.; Aguilar, J.A.; Ahlers, M.; Ahrens, M.; Altmann, D.; Anderson, T.; Arguelles, C.; Arlen, T.C.; et al. Observation of high-ener gy astrophysical neutrinos in three years of IceCube data. *Phys. Rev. Lett.* **2014**, *113*, 101101. [CrossRef] [PubMed]
69. Abe, K.; Hayato, Y.; Iida, T.; Iyogi, K.; Kameda, J.; Koshio, Y.; Kozuma, Y.; Marti, L.; Miura, M.; Moriyama, S.; et al. Evidence for the appearance of atmospheric tau neutrinos in Super-Kamiokande. *Phys. Rev. Lett.* **2013**, *110*, 181802. [CrossRef]
70. Cowan, C.L., Jr.; Reines, F.; Harrison, F.B.; Kruse, H.W.; McGuire, A.D. Detection of the free neutrino: A confirmation. *Science* **1956**, *124*, 103–104. [CrossRef]
71. Wiebusch, C.H.V. The Detection of Faint Light in Deep Underwater Neutrino Telescopes. Ph.D. Dissertation, Department of Physics I RWTH Aachen University, Aachen, Germany, 1995.
72. Adrián-Martínez, S.; Al Samarai, I.; Albert, A.; André, M.; Anghinolfi, M.; Anton, G.; Anvar, S.; Ardid, M.; Astraatmadja, T.; Aubert, J.-J.; et al. Search for cosmic neutrino point sources with four years of data from the ANTARES telescope. *Astrophys. J.* **2012**, *760*, 53. [CrossRef]
73. Gaisser, T.K. Cosmic rays and particle physics. *Comments Nucl. Part. Phys.* **1982**, *11*, 25–39.
74. Patrignani, C.; Agashe, K.; Aielli, G.; Amsler, C.; Antonelli, M.; Asner, D.M.; Baer, H.; Banerjee, S.W.; Barnett, RM.; Basaglia, T. Review of Particle Physics. *Chin. Phys. C* **2016**, *40*, 100001. https://iopscience.iop.org/article/10.1088/1674-1137/40/10/100001. [CrossRef]
75. Lee, T.D.; Yang, C.N. Question of parity conservation in weak interactions. *Phys. Rev.* **1956**, *104*, 254. [CrossRef]
76. Wu, C.S.; Ambler, E.; Hayward, R.W.; Hoppes, D.D.; Hudson, R.P. Experimental test of parity conservation in beta decay. *Phys. Rev.* **1957**, *105*, 1413. [CrossRef]
77. Coope, J.A.R.; Snider, R.F.; McCourt, F.R. Irreducible cartesian tensors. *J. Chem. Phys.* **1965**, *43*, 2269–2275. [CrossRef]
78. Coope, J.A.R.; Snider, R.F. Irreducible cartesian tensors. II. General formulation. *J. Math. Phys.* **1970**, *11*, 1003–1017. [CrossRef]
79. Coope, J.A.R. Irreducible Cartesian Tensors. III. Clebsch-Gordan Reduction. *J. Math. Phys.* **1970**, *11*, 1591–1612. [CrossRef]
80. Snider, R.F. *Irreducible Cartesian Tensors*; Walter de Gruyter GmbH and Co KG: Berlin, Germany, 2017; Volume 43.
81. Jackson, J.D. *Classical Electrodynamics*; John Wiley & Sons: Hoboken, NJ, USA, 2021.
82. Available online: https://en.wikipedia.org/wiki/Pauli_matrices (accessed on 21 August 2025).
83. Frankel, T. *The Geometry of Physics: An Introduction*; Cambridge University Press: Cambridge, UK, 2011.
84. Ryder, L.H. *Quantum Field Theory*; Cambridge University Press: Cambridge, UK, 1996.
85. Donoghue, J.F.; Golowich, E.; Holstein, B.R. *Dynamics of the Standard Model*; Cambridge University Press: Cambridge, UK, 2014; p. 573.
86. Born, M.; Oppenheimer, R. On the quantum theory of molecules. In *Quantum Chemistry: Classic Scientific Papers*; World Scientific: New Jersey, NJ, USA, 2000; pp. 1–24.
87. Mohapatra, R.N.; Pal, P.B. *Massive Neutrinos in Physics and Astrophysics*; World Scientific: New Jersey, NJ, USA, 2004; Volume 72.
88. Altarelli, G. The mystery of neutrino mixings. *arXiv* **2011**, arXiv:1111.6421. [CrossRef]
89. Fano, U. Description of states in quantum mechanics by density matrix and operator techniques. *Rev. Mod. Phys.* **1957**, *29*, 74. [CrossRef]
90. Wilde, M.M. *Quantum Information Theory*; Cambridge University Press: Cambridge, UK, 2013.
91. Fields, B.; Sarkar, S. Big-bang nucleosynthesis (particle data group mini-review). *arXiv* **2006**, arXiv:astro-ph/0601514. [CrossRef]
92. Peres, A. (Ed.) *Quantum Theory: Concepts and Methods*; Springer: Dordrecht, The Netherlands, 2002.
93. Hu, X.M.; Guo, Y.; Liu, B.H.; Li, C.F.; Guo, G.C. Progress in quantum teleportation. *Nat. Rev. Phys.* **2023**, *5*, 339–353. [CrossRef]
94. Bennett, C.H.; Brassard, G.; Crépeau, C.; Jozsa, R.; Peres, A.; Wootters, W.K. Teleporting an unknown quantum state via dual classical and Einstein-Podolsky-Rosen channels. *Phys. Rev. Lett.* **1993**, *70*, 1895. [CrossRef] [PubMed]
95. Shor, P.W. Algorithms for quantum computation: Discrete logarithms and factoring. In Proceedings of the IEEE 35th Annual Symposium on Foundations of Computer Science (FOCS), Santa Fe, NM, USA, 20–22 November 1994; pp. 124–134.
96. Levitt, M.H. *Spin Dynamics: Basics of Nuclear Magnetic Resonance*; John Wiley & Sons: Hoboken, NJ, USA, 2008.
97. Edmonds, A.R. *Angular Momentum in Quantum Mechanics*; Princeton University Press: Princeton, NJ, USA, 1996; Volume 4.
98. Guessoum, N.; Jean, P.; Gillard, W. The lives and deaths of positrons in the interstellar medium. *Astron. Astrophys.* **2005**, *436*, 171–185. [CrossRef]
99. Weidenspointner, G.; Skinner, G.; Jean, P.; Knödlseder, J.; Von Ballmoos, P.; Bignami, G.; Diehl, R.; Strong, A.W.; Cordier, B.; Schanne, S.; et al. An asymmetric distribution of positrons in the Galactic disk revealed by gamma-rays. *Nature* **2008**, *451*, 159–162. [CrossRef]
100. Beacom, J.F.; Bell, N.F.; Bertone, G. Gamma-ray constraint on Galactic positron production by MeV dark matter. *Phys. Rev. Lett.* **2005**, *94*, 171301. [CrossRef]

101. Steinberg, A.M. Quantum Measurements: A modern view for quantum optics experimentalists. *arXiv* **2014**, arXiv:1406.5535. [CrossRef]
102. Whitesides, G.M.; Grzybowski, B. Self-assembly at all scales. *Science* **2002**, *295*, 2418–2421. [CrossRef]
103. Doherty, M.W.; Manson, N.B.; Delaney, P.; Jelezko, F.; Wrachtrup, J.; Hollenberg, L.C. The nitrogen-vacancy colour centre in diamond. *Phys. Rep.* **2013**, *528*, 1–45. [CrossRef]
104. Taylor, J.M.; Cappellaro, P.; Childress, L.; Jiang, L.; Budker, D.; Hemmer, P.R.; Yacoby, A.; Walsworth, R.; Lukin, M.D. High-sensitivity diamond magnetometer with nanoscale resolution. *Nat. Phys.* **2008**, *4*, 810–816. [CrossRef]
105. Abi, B.; Albahri, T.; Al-Kilani, S.; Allspach, D.; Alonzi, L.P.; Anastasi, A.; Anisenkov, A.; Azfar, F.; Badgley, K.; Baeßler, S.; et al. Measurement of the positive muon anomalous magnetic moment to 0.46 ppm. *Phys. Rev. Lett.* **2021**, *126*, 141801. [CrossRef]
106. Aoyama, T.; Asmussen, N.; Benayoun, M.; Bijnens, J.; Blum, T.; Bruno, M.; Caprini, I.; Calame, C.C.; Cè, M.; Colangelo, G.; et al. The anomalous magnetic moment of the muon in the Standard Model. *Phys. Rep.* **2020**, *887*, 1–166. [CrossRef]
107. Moroi, T. Muon anomalous magnetic dipole moment in the minimal supersymmetric standard model. *Phys. Rev. D* **1996**, *53*, 6565. [CrossRef]
108. Gabrielse, G.; Hanneke, D.; Kinoshita, T.; Nio, M.; Odom, B. New Determination of the Fine Structure Constant from the Electron g Value and QED. *Phys. Rev. Lett.* **2006**, *97*, 030802. [CrossRef] [PubMed]
109. Mohr, P.J.; Taylor, B.N.; Newell, D.B. CODATA Recommended Values of the Fundamental Physical Constants. *Rev. Mod. Phys.* **2012**, *84*, 1527. [CrossRef]
110. Hestenes, D.; Lasenby, A. *Space-Time Algebra*; Springer International Publishing: Cham, Switzerland, 2015; p. 2015.
111. Bargmann, V.; Michel, L.; Telegdi, V.L. Precession of the Polarization of Particles Moving in a Homogeneous Electromagnetic Field. *Phys. Rev. Lett.* **1959**, 2, 435 [CrossRef]
112. Chiou, D.-W.; Chen, T.-W. Exact Foldy–Wouthuysen transformation of the Dirac–Pauli Hamiltonian. *arXiv* **2014**, arXiv:1405.4495.
113. Duval, C.; Horváthy, P.A. On the Bargmann–Michel–Telegdi equations, and spin–orbit coupling. *Nucl. Phys. B Proc. Suppl.* **2016**, *912*, 450–462. [CrossRef]
114. Foldy, L.L.; Wouthuysen, S.A. On the Dirac Theory of Spin 1/2 Particles and Its Non-Relativistic Limit. *Phys. Rev.* **1950**, 78, 29. [CrossRef]
115. Costella, J.P.; McKellar, B.H.J. The Foldy–Wouthuysen transformation. *Am. J. Phys.* **1995**, *63*, 1119. [CrossRef]
116. Silenko, A.J. General properties of the Foldy–Wouthuysen transformation and applicability of the corrected original method. *Phys. Rev. A* **2016**, *93*, 022108. [CrossRef]
117. KATRIN Collaboration; Aker, M.; Batzler, D.; Beglarian, A.; Behrens, J.; Beisenkötter, J.; Biassoni, M.; Bieringer, B.; Biondi, Y.; Block, F.; et al. Direct neutrino-mass measurement based on 259 days of KATRIN data. *Science* **2025**, *388*, 180–185. [CrossRef] [PubMed]
118. Freitas, A. TASI 2020 lectures on precision tests of the standard model. *arXiv* **2020**, arXiv:2012.11642. [CrossRef]
119. Erler, J.; Schott, M. Electroweak precision tests of the Standard Model after the discovery of the Higgs boson. *Prog. Part. Nucl. Phys.* **2019**, *106*, 68–119. [CrossRef]
120. Fan, X.; Myers, T.G.; Sukra, B.A.D.; Gabrielse, G. Measurement of the electron magnetic moment. *Phys. Rev. Lett.* **2023**, *130*, 071801. [CrossRef] [PubMed]
121. Lamb, W.E.; Retherford, R.C. Fine Structure of the Hydrogen Atom by a Microwave Method. *Phys. Rev.* **1947**, *72*, 241. [CrossRef]
122. Casimir, H.B.G. On the Attraction Between Two Perfectly Conducting Plates. *Proc. K. Ned. Akad. Wet.* **1948**, *51*, 793.
123. Penrose, R. Twistor algebra. *J. Math. Phys.* **1967**, *8*, 345–366. [CrossRef]
124. Penrose, R. Solutions of the Zero-Rest-Mass Equations. *J. Math. Phys.* **1969**, *10*, 38–39. [CrossRef]
125. Wikipedia: Physics Beyond the Standard Model. Available online: https://en.wikipedia.org/w/index.php?title=Physics_beyond_the_Standard_Model&oldid=1308782205 (accessed on 21 August 2025).
126. Wheeler, J.A.; Zurek, W.H. (Eds.) The Physical Content of Quantum Kinematics and Mechanics. In *Quantum Theory and Measurement*; Princeton University Press: Princeton, NJ, USA, 1983; pp. 62–68. (In English)
127. Albert Einstein, Delivered in a 1933 Lecture at Oxford Titled "On the Method of Theoretical Physics". Available online: https://eclass.uoa.gr/modules/document/file.php/PHS539/ (accessed on 5 April 2025).
128. Newton, I. *The Principia: Mathematical Principles of Natural Philosophy*; Cohen, I.B., Whitman, A., Translators; University of California Press: Berkeley, CA, USA, 1999.
129. "Interpretations of Quantum Mechanics," Wikipedia. The Free Encyclopedia. Available online: https://en.wikipedia.org/wiki/Interpretationsofquantummechanics (accessed on 5 April 2025).
130. Hall, B.C. Lie groups, Lie algebras, and representations. In *Quantum Theory for Mathematicians*; Springer: New York, NY, USA, 2013; pp. 333–366.

131. Georgi, H. *Lie Algebras in Particle Physics: From Isospin to Unified Theories*; Taylor & Francis: Abingdon, UK, 2000; p. 340.
132. Cornwell, J.F. *Group Theory in Physics*; Academic Press: Cambridge, MA, USA, 1984